PCCP

PAPER

View Article Online
View Journal

Cite this: DOI: 10.1039/d6cp00492j

Surface reactions of iron precursors for focused electron beam induced deposition revealed by reflection absorption infrared spectroscopy

Lars Barnewitz, [a] Hannah Boeckers, [a] Atul Chaudhary, [b] Lisa McElwee-White [b] and Petra Swiderek *[b]

This study compares the thermal surface chemistry of $Fe(CO)_5$, $Fe(CO)_4A$ (A = acrolein), and $Fe(CO)_4MA$ (MA = methyl acrylate) on Fe seed deposits produced by electron beam induced deposition (EBID) under UHV conditions. The deposits were prepared from $Fe(CO)_5$ by continuous vapour dosing and simultaneous electron irradiation. Annealing to 450 K resulted in the removal of remaining CO from the surface. Reflection absorption infrared spectroscopy (RAIRS) showed continuous thermal reactions when $Fe(CO)_5$ was dosed onto the deposit at room temperature. The characteristic $\nu(C{\equiv}O)$ bands were red shifted and broadened with increasing precursor dosage indicative of Fe aggregation. In comparison, vapour dosing of $Fe(CO)_4A$ and $Fe(CO)_4MA$ at room temperature produced a non-reactive monolayer coverage on the deposit. This fundamental difference in thermal surface chemistry is explained by a dissociative adsorption process of $Fe(CO)_4A$ and $Fe(CO)_4MA$, which leads to chemisorbed species that suppress autocatalytic growth of Fe from the precursors. The thermal decomposition at monolayer coverage occurs even at temperatures as low as 115 K. Dosing of $Fe(CO)_5$ on the chemisorbed adsorbates of $Fe(CO)_4A$ and $Fe(CO)_4MA$ also resulted in negligible thermal growth, as shown by Auger electron spectroscopy (AES) and RAIRS. Electron irradiation of the adsorbate did not reactivate the surface towards thermal decomposition of $Fe(CO)_5$. The results show that the replacement of one CO ligand by an organic ligand A or MA can efficiently inhibit thermal deposit growth. The novel precursors $Fe(CO)_4A$ and $Fe(CO)_4MA$ can thus improve the control over the deposit shape in focused electron beam-induced deposition (FEBID) processes.

Received 10th February 2026,
Accepted 25th March 2026

DOI: 10.1039/d6cp00492j

rsc.li/pccp

1 Introduction

Focused electron beam induced deposition (FEBID) is a state-of-the-art additive nanofabrication process. It relies on the electron-driven decomposition of precursor molecules by the tightly focused beam of a scanning electron microscope to write arbitrarily shaped structures on a supporting surface.[1–4] The precursor molecules are typically metal complexes with ligands that provide the compound with a sufficient volatility to be dosed onto the surface *via* a gas inlet system.[1–8] In the ideal case, only the central metal atom will remain on the surface, while the ligands are quantitatively converted to products that desorb from the surface. The electron-induced reactions of diverse precursors have thus been investigated and strategies for the design of ligand architectures have been derived that should enable optimal precursor fragmentation.[5–8]

The chemistry involved in FEBID is complex and complete fragmentation of the precursor alone does not guarantee that only the metal will be deposited. In the simplest case, the deposition process is governed by the adsorption–desorption equilibrium of the precursor, precursor diffusion, the electron-induced dissociation of the precursor, and by the probability that dissociation products desorb.[1,3] If products originating from the ligands do not desorb fast enough, unwanted elements are incorporated in the deposited material. In reality, though, not only electron-induced precursor dissociation but also thermal reactions can contribute to formation of deposits during FEBID processes. While thermal autocatalytic reactions may even lead to high-purity deposits,[9–12] they also compromise the spatial control inherent in FEBID because deposition is then governed by the surface temperature instead of the electron beam.[13,14] Strategies to suppress unwanted thermal deposition based upon a fundamental understanding and control of thermal surface reactions are therefore needed to

[a] *Institute for Applied and Physical Chemistry (IAPC), Faculty 2 (Chemistry/Biology), University of Bremen, Leobener Str. 5, 28359 Bremen, Germany. E-mail: swiderek@uni-bremen.de*
[b] *Department of Chemistry, University of Florida, Gainesville, Florida 32611, USA*

develop optimized FEBID processes. Thermal surface reactions are also of central relevance to novel hybrid approaches in nanostructure fabrication.[15] In these processes, a nanodevice is fabricated by FEBID and then coated with a conformal layer of a different material using chemical vapour deposition (CVD)[16] or atomic layer deposition (ALD)[17] with the aim of providing the device with protection or mechanical strength. In such processes, efficient adsorption of the precursor molecules and, in ALD, also self-limiting formation of a monolayer on the surface of the FEBID structure is needed. Again, an understanding of how the precursor molecules interact with the surface of the deposit prepared by FEBID is necessary to advance these processes. Finally, surface reactions may also be involved when FEBID leads to complex deposits composed of layers with different compositions as observed previously in the deposition of Ag.[18] Again, a detailed understanding of surface reactions may turn out to be the key to provide explanations for these results.

Despite the relevance of thermal surface chemistry in FEBID processes, research related to FEBID has so far not paid much attention to the nature of precursor interactions with a deposit. In fact, the surface chemistry of many common FEBID precursors has not been investigated so far.[3] Instead, surface science studies have often focused on prototypical molecules such as $Fe(CO)_5$ and mainly concerned the thermal chemistry that occurs upon adsorption on single-crystal metal surfaces.[19–26] Therefore, we have recently started to investigate the electron beam induced deposition (EBID) and thermal reactions of Fe precursors on the surface of the resulting deposits by surface science techniques.[27,28] In our work, the term EBID is used instead of FEBID because surface science experiments use a defocused electron source to irradiate the entire surface for optimum sensitivity in the detection of reaction products.[3,29,30] This has, for instance, provided evidence that adsorption of NH_3 on an Fe deposit prepared by EBID can inhibit thermal autocatalytic growth of Fe from $Fe(CO)_5$.[27] However, this inhibition was not observed on the much purer Fe layers produced by thermal growth[27] in line with earlier reports that oxygen impurities on Fe surfaces increase the binding strength of NH_3.[31] This result clearly supports that studies that employ deposits akin to those prepared by FEBID are of key relevance to the understanding of the actual FEBID processes.

As an alternative strategy to suppress autocatalytic growth, the outcome of EBID and of thermal growth on an Fe deposit were recently studied using the novel precursor iron tetracarbonyl methyl acrylate ($Fe(CO)_4MA$, MA = methyl acrylate, Fig. 1(a)).[28] Comparison of data from Auger electron spectroscopy (AES) with analogous experiments for $Fe(CO)_5$ showed that the organic ligand in fact suppresses thermal growth. Still, EBID using $Fe(CO)_4MA$ yielded deposits with surprisingly low carbon content which was only about 50% higher than found in EBID experiments conducted with $Fe(CO)_5$.[28] While this is a promising result, molecular insight in the details of the underlying surface chemistry was so far missing. Therefore, we report herein a study by reflection absorption infrared spectroscopy (RAIRS) regarding the surface chemistry of $Fe(CO)_5$, $Fe(CO)_4MA$,

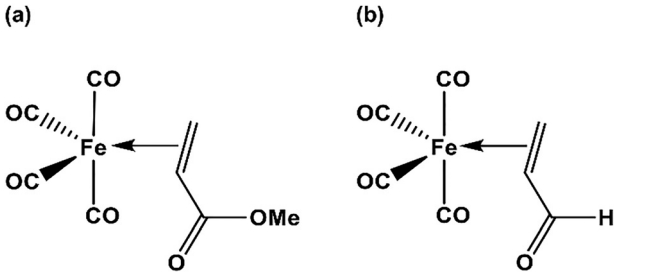

Fig. 1 Molecular structures of (a) iron tetracarbonyl methyl acrylate ($Fe(CO)_4MA$) and (b) iron tetracarbonyl acrolein ($Fe(CO)_4A$).

and the novel precursor iron tetracarbonyl acrolein ($Fe(CO)_4A$, A = acrolein, Fig. 1(b)) on a deposit prepared by EBID using $Fe(CO)_5$ as precursor. For reference, we first summarize infrared spectroscopic data of $Fe(CO)_5$ and previous studies on its adsorption on single crystal surfaces (Section 3.1). Next, insight into the formation of the deposit by EBID is discussed (Section 3.2) followed by results on the surface chemistry at cryogenic temperature and at room temperature obtained from $Fe(CO)_5$ (Section 3.3) and from the novel precursors $Fe(CO)_4MA$ and $Fe(CO)_4A$ (Section 3.4). Finally, we present AES data showing that adsorption of $Fe(CO)_4MA$ and $Fe(CO)_4A$ inhibits subsequent thermal growth of Fe from $Fe(CO)_5$ and reveal the origin of this effect by RAIRS (Section 3.5).

2 Experimental

2.1 Precursors

$Fe(CO)_5$ was purchased from Sigma-Aldrich (>99.99% purity). $Fe(CO)_4MA$ and $Fe(CO)_4A$ were synthesized in Gainesville. The procedures used to synthesize $Fe(CO)_4MA$ were described previously and the general procedures for synthesis of $Fe(CO)_4A$ are as reported.[28] The latter complex was synthesized by a modification of a literature procedure.[32] A solution of $Fe_2(CO)_9$ (0.50 g, 1.4 mmol) in 30 mL of benzene was prepared in a 100 mL Schlenk flask inside a nitrogen-filled glovebox. To this solution, acrolein (0.091 mL, 1.37 mmol) was then added, and the reaction mixture was stirred overnight at 35 °C. The solvent was subsequently removed under vacuum using standard Schlenk techniques. The crude product was purified by sublimation at 28 °C and 112 mTorr overnight, resulting in yellowish solid product (120.0 mg, 39%). The product was characterized by comparison to literature data[32] using infrared (IR) and ^1H NMR spectroscopy as follows. IR (hexanes) ν_{CO}: 2100, 2039, 2022, 2002 cm^{-1}. ^1H NMR (400 MHz, $CDCl_3$) δ 9.04 (d, J = 5.2 Hz, 1H), 3.66 (ddd, J = 12.2,7.4,5.2 Hz, 1H), 2.76–2.73 (m, 2H).

2.2 Ultrahigh vacuum (UVH) setup

Experiments were performed in an UHV setup located in Bremen.[27,28] It operates at a base pressure of 10^{-10} mbar and is equipped with a polycrystalline Ta sheet as a substrate. The setup comprises two chambers separated by a gate valve, between which the Ta sheet can be transferred vertically. The upper chamber was used for AES (STAIB DESA 100) and

cleaning of the Ta sheet with a sputter gun operated with Ar^+ ions at an energy of 3 keV. Before each experiment, sputtering was performed for 30–60 min to remove any residual species from the Ta sheet as monitored by AES. The lower chamber is equipped with a quadrupole mass spectrometer (QMS) residual gas analyser (Stanford, 300 amu) using electron ionization at an energy of 70 eV for detection of neutral species, as well as a commercial flood gun (SPECS FG 15/40) for electron irradiation. It is also coupled to an infrared spectrometer (IFS 66 v/S, Bruker) allowing to perform RAIRS on the Ta sheet at grazing incidence. The defocused electron gun irradiates the entire Ta substrate with an area of 5 cm^2. The Ta sheet is cooled to (115 ± 3) K (stated as 115 K further on) by a liquid nitrogen-cooled bath cryostat. Two thin Ta ribbons spot-welded to the thicker Ta sheet are used for resistive heating. The precursor vapours were introduced into the UHV chamber *via* a stainless-steel tube with an opening pointing toward the Ta surface. This results in an effusive molecular beam, which is divergent enough to fully cover the entire Ta sheet during precursor deposition. The amount of dosed vapour was defined by measuring the pressure drop in the gas inlet manifold in units of mTorr with a capacitance manometer when leaking the precursors onto the Ta sheet.

2.3 Thermal desorption spectroscopy (TDS)

Before dosing the precursors, a bake-out of the Ta sheet at 450 K was performed for 30 s to remove adsorbed residual gases. TDS experiments were used to monitor volatile molecules that were thermally desorbed from the surface. To this end, characteristic *m*/*z* ratios were recorded using the QMS during heating at a constant heating rate of 1 K s^{-1}. Previous TDS experiments[27,28] have revealed that a pressure drop in the gas handling manifold of approximately 1 mTorr results in monolayer coverages of $Fe(CO)_5$ and $Fe(CO)_4MA$. This estimate was obtained by dosing varying amounts of the precursors onto the Ta substrate and recording TDS curves for specific *m*/*z* ratios (*m*/*z* 28, 55, 56) indicative of the precursors. A similar result was obtained for $Fe(CO)_4A$ (see SI, Fig. S1). Therefore, coverages stated below are denoted as *n* monolayers (*n* ML). TDS experiments were also used to monitor the thermally induced changes of the precursor adsorbates. In this case, TDS was performed in steps of 50 K with each step being followed by acquisition of a RAIR spectrum. After reaching 450 K, the surface was held at this temperature for another 30 s to remove remaining adsorbed material.

2.4 Reflection absorption infrared spectroscopy (RAIRS)

RAIR spectra were recorded by accumulating 400 individual scans with a resolution of 4 cm^{-1} and an aperture of 2.0 mm over a wavenumber range of 4000 cm^{-1} to 420 cm^{-1} using a liquid nitrogen-cooled MCT (mercury cadmium telluride) narrow-band detector with a sensitivity down to 850 cm^{-1}. Prior to measurements, the spectrometer was purged with N_2 gas and then evacuated. When RAIR spectra were recorded continuously over longer time periods, the time interval between measurements was set to 60 s, which roughly corresponds to the time needed for a single spectrum and thus allowed for continuous monitoring of the chemical processes. Background spectra were either acquired at the beginning of an experimental sequence or prior to individual steps of an experiment as stated in the captions to the figures.

2.5 Auger electron spectroscopy (AES)

AES was used to characterize deposits resulting from EBID and subsequent thermal reactions and to confirm the absence of Fe after sputter cleaning of the substrate. Spectra were recorded at room temperature with an incident energy of 5 keV while pulse counting in the fixed retarding ratio (FRR) mode with a variable energy resolution of dE/E = 0.6%. The measurement took around 60 min accumulating 100 scans in the energy range between 100 eV and 800 eV with a beam current measured on the surface of about 300 nA. To avoid beam damage when measuring multiple spectra in one experiment, the position of the Ta sheet was altered for each sequential experiment step since the beam spot size is about 1 mm in diameter. The obtained direct AES data was baseline corrected by using the asymmetric least squares method and smoothed with a Savitzky–Golay filter. Afterwards, the AES data was numerically differentiated with respect to the electron energy to derive peak-to-peak heights.

2.6 Preparation of deposits by EBID and adsorption of precursor layers

After receiving the shipped precursors $Fe(CO)_4A$ and $Fe(CO)_4MA$ in Bremen they were transferred into a glass reservoir with Ar atmosphere. The reservoirs were mounted to the gas inlets of the UHV chamber. After freezing the solid precursors with liquid nitrogen, the valves to the pump were opened to pump Ar out of the reservoirs until no pressure increase was measurable in the gas inlet. Afterwards, the precursors were brought to room temperature and shortly pumped again to remove residual gases. $Fe(CO)_5$ was degassed by multiple freeze–pump–thaw cycles.

Deposits for subsequent studies of precursor adsorption were prepared by EBID, which was performed by simultaneous electron irradiation and dosing of $Fe(CO)_5$ onto on the freshly sputtered Ta substrate held at room temperature. The pressure drop in the gas inlet during an EBID process always amounted to 5 mTorr. Electron irradiation was performed with an energy of 50 eV and a total exposure of 10 000 μC cm^{-2}, which was achieved after (530 ± 5) s. The impinging electron current was roughly constant during the entire irradiation period. Precursor dosage started at the beginning of the irradiation and always terminated before the final electron exposure was reached. The times needed to dose the entire amount of gas, however, varied between 80 s and 450 s. The progress of the reactions during EBID was monitored by repeated RAIRS measurements in which each spectrum covers approximately a 60 s timeframe. After electron irradiation, the deposit was annealed to 450 K using the stepwise approach described in Section 2.3. Each heating step was followed by a RAIRS measurement to analyze the thermally induced changes to the deposit.

The adsorption and thermal reactions of the three precursors $Fe(CO)_5$, $Fe(CO)_4A$, and $Fe(CO)_4MA$ on the deposits prepared by

EBID at 115 K, upon stepwise annealing, and at room temperature was again monitored by RAIRS. The details of these experiments are given below.

3 Results and discussion

3.1 Reference data on $Fe(CO)_5$ adsorbates

This section summarizes fundamental data on the infrared spectra of $Fe(CO)_5$ and its adsorbates as relevant for the discussion of the results described further on. A more comprehensive overview can be obtained from the cited references. Isolated $Fe(CO)_5$ molecules have a trigonal bipyramidal geometry and thus D_{3h} symmetry. Among the five C≡O stretching vibrations, only the asymmetric axial $A''_{2,ax}$ and the degenerate equatorial E'_{eq} vibrations are infrared active.[33] They are observed at 2034 cm^{-1} and 2012–2014 cm^{-1} in the gas phase or at 2023 cm^{-1} and 1996 cm^{-1} for $Fe(CO)_5$ embedded in Xe matrices.[19,34]

Multilayer $Fe(CO)_5$ adsorbates can be grown at liquid nitrogen temperature. The RAIR spectra of such adsorbates are dominated by a strong and sharp ν(C≡O) band at or near 2065 cm^{-1}, which is assigned to the asymmetric axial $A''_{2,ax}$ vibration.[19–25,34] The equatorial E'_{eq} vibrations appear with low intensity at or near 2015 cm^{-1}.[20,34] The intense $A''_{2,ax}$ vibration exhibits a particularly large shift towards higher wavenumbers as compared to the gas phase.[19] This is explained by dipole coupling between aligned $Fe(CO)_5$ molecules in the dense adsorbate layer.[24,34] Furthermore, the strong dominance of the axial $A''_{2,ax}$ vibration over the equatorial E'_{eq} band is in stark contrast to the IR spectrum obtained, for instance, in Xe matrix where both bands have comparable intensities.[34] This is traced back to an orientation effect as illustrated for $Fe(CO)_5$ adsorbed on an alkanethiol self-assembled monolayer (SAM) on a Au substrate.[34] The SAM is an inert support so that $Fe(CO)_5$ adsorbs as undistorted species in the monolayer. However, at low coverage, the RAIR spectrum of $Fe(CO)_5$ on the SAM shows the $A''_{2,ax}$ and the E'_{eq} vibration with similar intensities while only the $A''_{2,ax}$ band continues to grow with increasing multilayer coverage.[34] Based on the surface selection rule of RAIRS,[35] this was interpreted in terms of a tilted orientation of the trigonal axis of $Fe(CO)_5$ in the monolayer while molecules in the multilayer adsorb with the same axis perpendicular to the surface.[34] The same upright orientation can also explain the strong dominance of the $A''_{2,ax}$ vibration in RAIR spectra of multilayer $Fe(CO)_5$ on metal surfaces such as Au(111),[20] Ag(111),[21] an Fe fcc layer,[23] as well as on a SiO_2 layer.[22]

In contrast to the situation on an organic layer,[34] adsorption at monolayer coverage on metal surfaces, again studied at liquid nitrogen temperature, often leads to distortion or even dissociation of $Fe(CO)_5$ because of stronger interactions with the metal. A slight distortion of $Fe(CO)_5$ from the D_{3h} geometry causes the infrared forbidden symmetric equatorial vibration $A'_{1,eq}$ to acquire some intensity. This signal shows up at 2113 cm^{-1} on Au(111)[20] and Ag(111)[21] or at 2120 cm^{-1} on an Fe fcc layer.[23] It disappears, however, when the Au(111) surface is precovered by monolayer amounts of *n*-decane[20] giving evidence that the interaction with the metal induces the observed distortion of adsorbed $Fe(CO)_5$. Adsorption on Pt(111) leads to partial dissociation already at liquid nitrogen temperature as evident from a signal around 2100 cm^{-1} ascribed to CO bound to the Pt(111) surface.[19] An additional signal at 2065 cm^{-1} at monolayer coverage was ascribed to $Fe(CO)_5$, which was proposed to assume a D_{4h} geometry with square planar base parallel to the surface and an apical ligand perpendicular to the surface.[19] The latter would be infrared active according to the surface selection rule. The study also showed that adsorption at room temperature leads to quantitative dissociation on Pt(111).[19]

The reactivity of Fe surfaces is of particular relevance to the present study. It has been shown to depend on the type of surface as prepared by deposition of Fe vapour onto different single crystalline supports.[23] At liquid nitrogen temperature, $Fe(CO)_5$ adsorbs intact but slightly distorted on the fcc Fe(100) surface as deduced from a main band at 2060 cm^{-1} $\left(A''_{2,ax}\right)$ and a shoulder around 2000 cm^{-1} $\left(E'_{eq}\right)$.[23] The E'_{eq} signal implies that the trigonal axis is not exactly perpendicular to the surface. An additional small signal at 2120 cm^{-1} $\left(A'_{1,eq}\right)$ points again to a somewhat distorted geometry.[23] Upon photolysis, the main band shifted to 2072 cm^{-1} while the 2120 cm^{-1} signal disappeared, which was tentatively ascribed to formation of $Fe(CO)_4$.[23] In contrast, only the signal at 2072 cm^{-1} was observed upon adsorption on a bcc Fe surface pointing to immediate dissociation.[23] An earlier study using an Fe layer with lack of crystallographic order revealed the dominant signal of the multilayer $Fe(CO)_5$ adsorbate at 2065 cm^{-1} $\left(A''_{2,ax}\right)$ and a monolayer signal with low intensity ascribed to $A'_{1,eq}$ at 2125 cm^{-1}.[24] Photolysis of the multilayer $Fe(CO)_5$ adsorbate caused decay of $Fe(CO)_5$ signals and appearance of a band at 2080–2084 cm^{-1}, again ascribed to $Fe(CO)_4$.[24] Heating to 270 K after photolysis shifted the main bands to 2050 cm^{-1}. This was proposed to relate to formation of $Fe_3(CO)_{12}$ (compare below).[24] For comparison, the vibrational signals of CO adsorbed at coverages above 0.5 monolayers were reported as 1985 cm^{-1} on Fe(110) and 1850 cm^{-1} and 2000 cm^{-1} on Fe(111).[36] A more detailed study on the adsorption of CO was performed on a fcc Fe(100) layer with thickness of 8 ML grown epitaxially on Cu(100).[37] The results revealed the adsorption of CO on different sites with ν(C≡O) bands shifting from 1920 cm^{-1} to 1998 cm^{-1} with increasing coverage for bridging adsorption and from 2020 cm^{-1} to around 2050 cm^{-1} for on-top adsorption sites.[37] We note that the reactivity of Fe surfaces towards $Fe(CO)_5$ is also evident from the fact that $Fe(CO)_5$ undergoes autocatalytic decomposition at room temperature leading to an Fe deposit with high purity.[10,13] This growth is enabled by desorption of CO, which provides sites for adsorption and dissociation of further $Fe(CO)_5$.[26]

Overall, the identification of the intermediate $Fe(CO)_4$ from surface science experiments is not trivial. Evidence for the

formation of a product with Fe : CO ratio of 4 was obtained by XPS after the multilayers of $Fe(CO)_5$ had been desorbed from a Ag surface.[25] Desorption experiments demonstrated that photolysis of $Fe(CO)_5$ on Ag(111) led to a product with the same average composition.[21] On the other hand, a direct identification of $Fe(CO)_4$ by RAIRS is complicated by the fact that the vibrational frequencies depend on the binding strength between the Fe atom and the respective surface and on the resulting structure of the intermediate. Therefore, assignments of vibrational signals to $Fe(CO)_4$ (2035 cm^{-1} on Pt(111),[19] 2081 cm^{-1} on Au(111),[20] 2052 cm^{-1} on a Ag sheet,[25] 2058 cm^{-1} or 2068 cm^{-1} on Ag(111),[21] 2084 cm^{-1} on a disordered Fe surface,[24] 2072 cm^{-1} on fcc or bcc Fe surfaces[23]) were generally considered as tentative. We note, however, that $Fe(CO)_4$ has also been observed, together with $Fe(CO)_4^-$, as the most abundant products when a mixture of $Fe(CO)_5$ and a rare gas was exposed to an electron beam with energies in the range 150–300 eV and then frozen on an IR window held at 16 K so that reactive intermediates became trapped.[38] Also, loss of a single CO ligand is the dominant outcome of dissociative electron attachment to $Fe(CO)_5$.[39,40]

The intermediate $Fe(CO)_4$ that results from the first loss of CO from $Fe(CO)_5$ can undergo further reactions. Different products were identified by IR spectroscopy. For instance, formation of $Fe_2(CO)_9$ was deduced from the appearance of signals at 2063.5 cm^{-1} and 2040.9 cm^{-1} when an Ar matrix containing $Fe(CO)_5$ and both trapped $Fe(CO)_4$ and $Fe(CO)_4^-$ was annealed.[38] The band positions are in line with the spectrum of $Fe_2(CO)_9$ co-condensed with an excess of Ar at 20 K that showed very strong bands at 2066 cm^{-1} and 2038 cm^{-1} as well as a band with medium intensity near 1850 cm^{-1}.[41] The former two bands are ascribed to the terminal CO ligands while the low wavenumber band relates to the bridging CO ligand.[42] The bridging CO was not reported from the annealing experiment,[38] most likely due to overlap with bands ascribed to $Fe(CO)_4^-$. We note that during annealing, bands ascribed to $Fe(CO)_4^-$ decayed more strongly than those assigned to $Fe(CO)_4$.[38] Formation of $Fe_2(CO)_9$ thus more likely results from a reaction of $Fe(CO)_4^-$ than of $Fe(CO)_4$.

$Fe_3(CO)_{12}$ instead of $Fe_2(CO)_9$ was identified from the appearance of a band at 2052 cm^{-1} when $Fe(CO)_5$ adsorbed on silica particles was subject to photolysis at temperatures ranging from 100 K to 300 K and it was demonstrated that $Fe(CO)_4$ was produced as well.[43] The new band agrees well with the IR spectrum of pure $Fe_3(CO)_{12}$ in an Ar matrix with most intense bands at 2056 cm^{-1} and 2051 cm^{-1} as well as 2036 cm^{-1}.[44] The latter band overlaps with the signals of $Fe(CO)_5$ on the silica particles (2024 cm^{-1} and 2002 cm^{-1}) so that it could not be observed as a new product band.[43] We note that $Fe_2(CO)_8$ was observed upon photolysis of $Fe_2(CO)_9$ in rare gas matrices.[41] The product consisted of two different isomers with dominant IR bands either at 2050–2060 cm^{-1} and ~2030 cm^{-1} or at ~2040 cm^{-1} and ~2008 cm^{-1}.[41]

Electron irradiation as used to prepare deposits by EBID can also convert $Fe(CO)_5$ to cationic species. The vibrational bands of cationic carbonyl complexes are typically located at higher wavenumbers than those of neutral species.[45] Characteristic bands of the radical cation $Fe(CO)_5^{+\bullet}$ have been reported above 2100 cm^{-1}.[46] The same applies to different cationic fragments as deduced from matrix isolation studies.[47,48]

We emphasize again that the positions of strong bands in RAIR spectra of adsorbates on metals are subject to orientation and dipole coupling effects that are absent in matrices. This must be considered in the interpretation of the RAIRS results presented further on.

3.2 Electron beam induced deposition of Fe-containing layers

The aim of the present study is to reveal thermal surface chemistry that contributes to FEBID processes. For a realistic insight, the reactions are studied on deposits prepared by EBID using $Fe(CO)_5$ as precursor as described in Section 2.6. The formation of these deposits is discussed here. Fig. 2 shows representative RAIRS results of EBID processes obtained by slow and rapid precursor dosing. A sharp band with maximum at 2060 cm^{-1} in the earlier RAIR spectra of each EBID process is ascribed to adsorbed $Fe(CO)_5$ (compare Section 3.1). When the total amount of $Fe(CO)_5$ was dosed slowly during 310 s (60% of the irradiation period), this signal reached its maximum intensity during the second RAIRS scan recorded between 60 s and 120 s of the deposition process. It then remained stable throughout the next two scans due to the continued precursor replenishment before starting to decay (Fig. 2(a)). A shoulder appeared towards lower wavenumbers and developed into a broad band with maximum located around 2000 cm^{-1}. This value is already close to the vibrational signals of CO on Fe(110) and Fe(111) surfaces.[36] The broadness of the CO stretching band observed after the EBID process, however, points to a superposition of different bonding situations as described previously[37] and possibly including Fe aggregates of various sizes and bridging CO ligands (compare Section 3.1). Contributions of cationic species are excluded because those would be expected at higher wavenumbers[45–48] and such charged species may be prone to neutralization on a conductive surface as used in the present experiments. We also note that according to AES, deposits obtained from $Fe(CO)_5$ by EBID contain oxygen and carbon.[27,28] An example is also included in the SI (Fig. S2). The co-deposition of oxygen and carbon presumably results from thermal or electron-induced dissociation of CO and contributes to the variety of binding sites.

When the total amount of $Fe(CO)_5$ was dosed rapidly within 90 s (17% of the irradiation period), the sharp peak at 2060 cm^{-1} had already reached its maximum intensity during the first RAIR spectrum and decayed after the second spectrum during which the precursor dosage was completed (Fig. 2(b)). Again, a shoulder appeared towards lower wavenumbers, which developed into a broad band with a maximum around 2030 cm^{-1} by the end of the electron irradiation. We propose from the smaller red shift with respect to the initial 2060 cm^{-1} band, that the aggregation was less extensive here. To support this conclusion, a second EBID process was performed, again with rapid dosing (100 s, 19% of the irradiation period), on the deposit resulting from the experiment shown in Fig. 2(b).

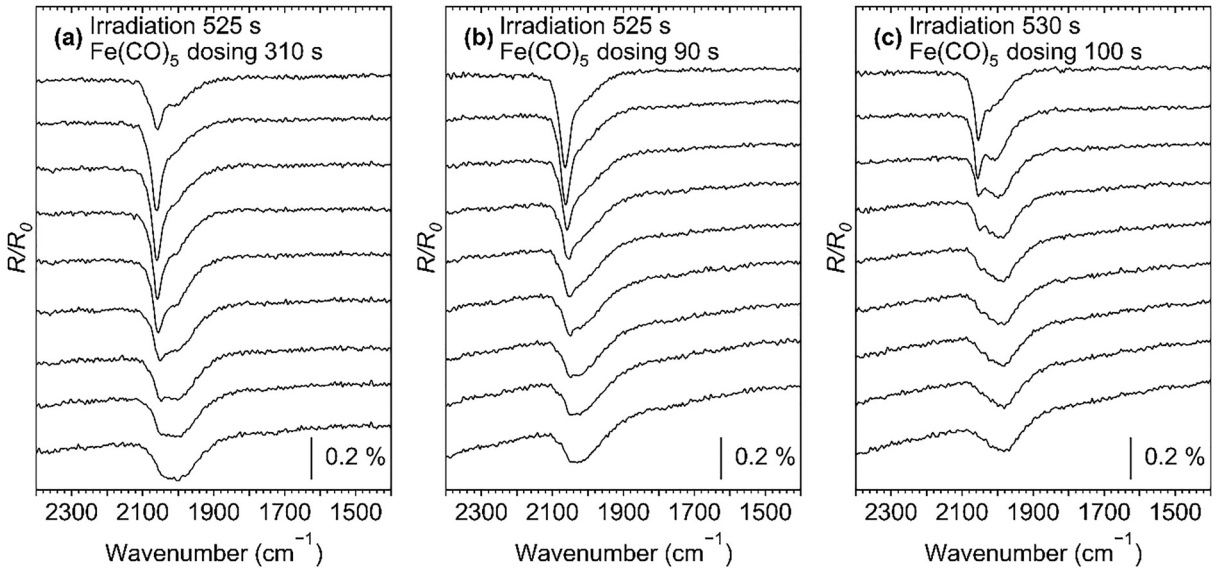

Fig. 2 RAIR spectra recorded during electron beam induced deposition (EBID) at room temperature on (a) and (b) a freshly sputter-cleaned Ta substrate and (c) on the deposit prepared in (b). Deposition was performed by dosing of $Fe(CO)_5$ onto the surface during electron irradiation (10 000 μC cm^{-2} at 50 eV). The total amount of $Fe(CO)_5$ vapour used in each frame would have produced a 5 ML adsorbate at 115 K (see Section 2.3). Each spectrum represents a time interval of roughly 60 s with increasing deposition time from top to bottom. All RAIR spectra of an individual frame are referenced to a background recorded prior to the start of EBID. The recording of the first spectrum started simultaneously with the beginning of the irradiation and $Fe(CO)_5$ dosing. The last spectrum in each frame was recorded after electron irradiation was terminated. Irradiation and $Fe(CO)_5$ dosing lasted during (a) 525 s and 310 s, (b) 525 s and 90 s, (c) 530 s and 100 s.

In this case, the initial 2060 cm^{-1} peak had an overall lower intensity and the shoulder towards lower wavenumbers evolved more rapidly into a broad band with maximum around 1980 cm^{-1} at the end of the EBID process (Fig. 2(c)). As was shown previously, each EBID using $Fe(CO)_5$ leads to deposition of further Fe.[27,28] This supports that the stronger shift of the band maximum towards lower wavenumber in the second EBID process correlates with the degree of Fe aggregation.

To further support our conclusion, we consider that the total amount of $Fe(CO)_5$ vapour dosed during the EBID process would be sufficient to build up an adsorbate with an average coverage of roughly 5 ML on the substrate held at 115 K (see Section 2.3). However, the multilayer of $Fe(CO)_5$ desorbs below 170 K,[27] so that only a monolayer coverage of the order of 10^{14}–10^{15} molecules per cm^2 is expected in the EBID process performed at room temperature. In the present EBID experiments (Fig. 2), this coverage was maintained for a longer time when the precursor was dosed slowly compared to rapid dosing. Considering that the electron current was roughly constant throughout the irradiation period, slower dosing thus allowed more impinging electrons to interact with and dissociate an $Fe(CO)_5$ monolayer than in the case of rapid dosing. This implies that the deposition rate is determined by the electron current density (electron-limited regime[1,3]). The validity of this correlation is also confirmed by AES data. The intensity of the Fe_{LMM} signal after the first EBID step (I_{EBID}(Fe)) was normalized to the intensity of the respective Ta_{NNN} signal of the freshly sputtered surface prior to EBID (I_0(Ta)) and plotted against the duration of $Fe(CO)_5$ dosing during the EBID step for a larger number of experiments (Fig. 3). The data clearly show that

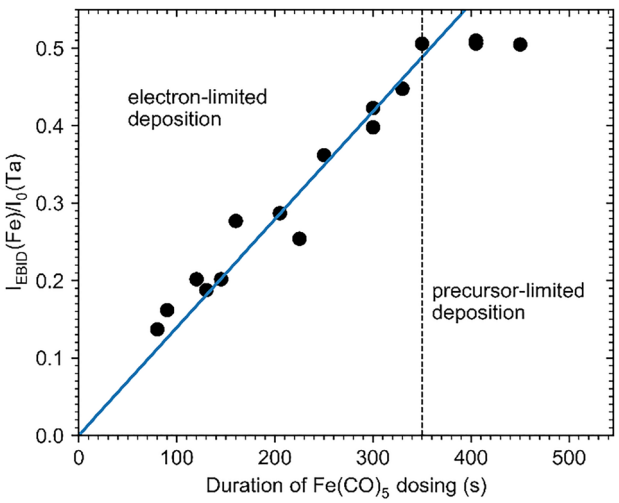

Fig. 3 Intensity of the Fe_{LMM} signal after the first EBID step normalized to the intensity of the Ta_{NNN} signal from the freshly sputtered surface prior to EBID as function of the duration of $Fe(CO)_5$ dosing during the EBID step. Data taken from 16 individual EBID experiments, each performed by dosing of $Fe(CO)_5$ onto the surface during electron irradiation (10 000 μC cm^{-2} at 50 eV, lasting for (530 ± 5) s). The total amount of $Fe(CO)_5$ vapour used in each experiment would have produced a 5 ML adsorbate at 115 K (see Section 2.3).

the amount of deposited Fe increases with increasing duration of dosing. However, a tendency towards saturation of the AES signal is observed above 350 s. This saturation cannot be ascribed to an effect of the limited electron attenuation length within the deposit[28] because, as shown further on

(see Section 3.5), higher values of $I(\mathrm{Fe})/I_0(\mathrm{Ta})$ can be achieved after repeated deposition steps. We therefore propose that the transition from the linear increase of $I_{\mathrm{EBID}}(\mathrm{Fe})/I_0(\mathrm{Ta})$ to the constant value beyond 350 s, *i.e.* for particularly slow precursor dosing, marks the switch from an electron-limited to a precursor-limited deposition regime.[1,3] Beyond 350 s, the precursor flux is thus too slow to fully replenish the monolayer so that the maximum, *i.e.* electron-limited, deposition rate is not achieved anymore.

The RAIR spectra recorded during the EBID experiment (Fig. 2) show that significant amounts of CO remained adsorbed even at room temperature and after the precursor supply was terminated. CO was removed when the temperature was increased as evident from both RAIRS and TDS data (Fig. 4). Fig. 4(a) shows RAIR spectra that were recorded after annealing the deposit resulting from the EBID experiment presented in Fig. 2(a) to successively higher temperatures. At 350 K, the intensity of the broad $\nu(\mathrm{C}\equiv\mathrm{O})$ band around 2000 cm^{-1} has decreased somewhat (Fig. 4(a)) as compared to room temperature (Fig. 2(a), bottom). Most of the intensity was lost at 400 K and the signal vanished at 450 K (Fig. 4(a)). In line with this, the TDS data recorded during the three annealing steps (Fig. 4(b)) reveal that CO desorption sets in near room temperature but reaches its maximum rate at 360 K. We note that all subsequent experiments on the adsorption and thermal reactions of $\mathrm{Fe(CO)_5}$, $\mathrm{Fe(CO)_4A}$, and $\mathrm{Fe(CO)_4MA}$ were performed on Fe-containing deposits resulting from a single EBID step and annealed to 450 K prior to dosing of the precursors to remove remaining CO.

3.3 Surface chemistry of $\mathrm{Fe(CO)_5}$ on a deposit prepared by EBID

Impurities of oxygen and carbon (see SI Fig. S2) can have an effect on the surface chemistry of deposits prepared by EBID. Therefore, RAIRS was used to study the interaction of $\mathrm{Fe(CO)_5}$ with a deposit surface and the results are compared to previous data regarding the adsorption and reactions of $\mathrm{Fe(CO)_5}$ on pure Fe surfaces (see Section 3.1 and ref. 23 and 24). In a first experiment, small quantities of $\mathrm{Fe(CO)_5}$ were repeatedly dosed onto a deposit held at 115 K and a RAIR spectrum was recorded after each step (Fig. 5). The total amount of $\mathrm{Fe(CO)_5}$ vapour dosed in the experiment was sufficient to produce a 5 ML adsorbate as deduced previously from TDS experiments.[27,28] A new background spectrum was recorded prior to each dosing to visualize the different adsorption mode in the monolayer and the multilayer. An analogous experiment in which all RAIR spectra are referenced to the same background spectrum recorded prior to the first dosing is included in the SI (Fig. S3).

The RAIR spectrum recorded after the first dose of $\mathrm{Fe(CO)_5}$ vapour, yielding an approximate coverage of 0.5 ML, shows a broad $\nu(\mathrm{C}\equiv\mathrm{O})$ band with maximum at 2065 cm^{-1} and a shoulder at 2050 cm^{-1} (Fig. 5, 0.5 ML). The band positions agree well with those reported for about 0.5 ML of $\mathrm{Fe(CO)_5}$ on bcc and fcc Fe(100) surfaces (2066 cm^{-1} and 2053 cm^{-1}, respectively[23]), implying that differently structured adsorption sites are present on the deposit prepared by EBID. In addition, the weak $A'_{1,\mathrm{eq}}$ signal is observed at 2129 cm^{-1}, revealing a distorted adsorption geometry as described earlier.[20,21,24]

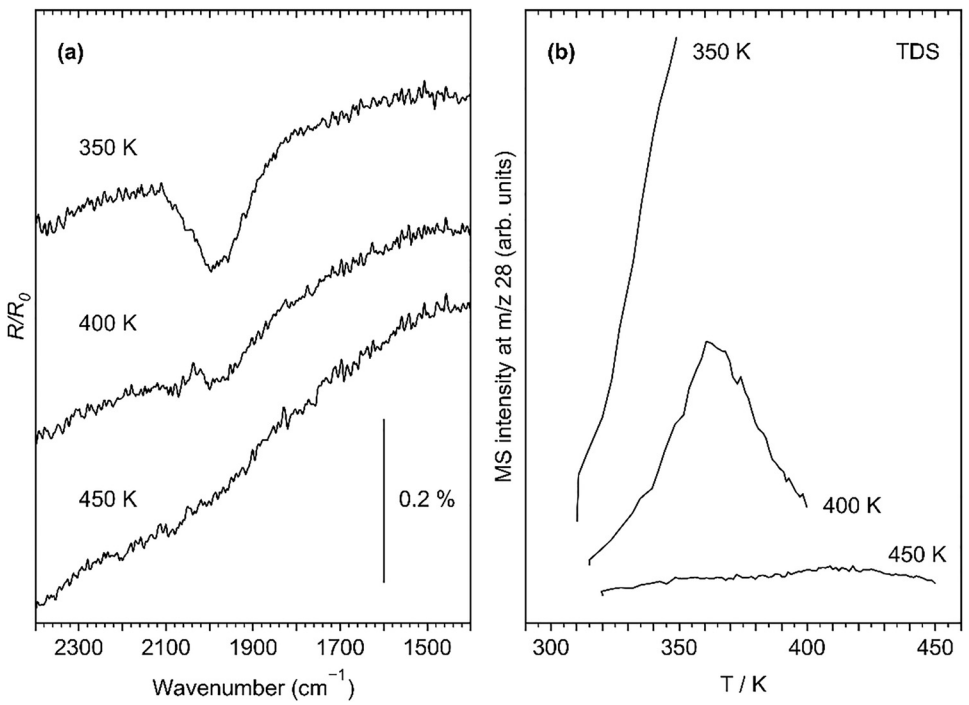

Fig. 4 (a) RAIR spectra recorded after annealing of the deposit prepared as shown in Fig. 2(a) to successively higher temperatures. The background was the same as used to record the data of Fig. 2(a). (b) TDS data recorded at *m*/*z* 28 during the annealing steps leading to the temperatures marked in (a).

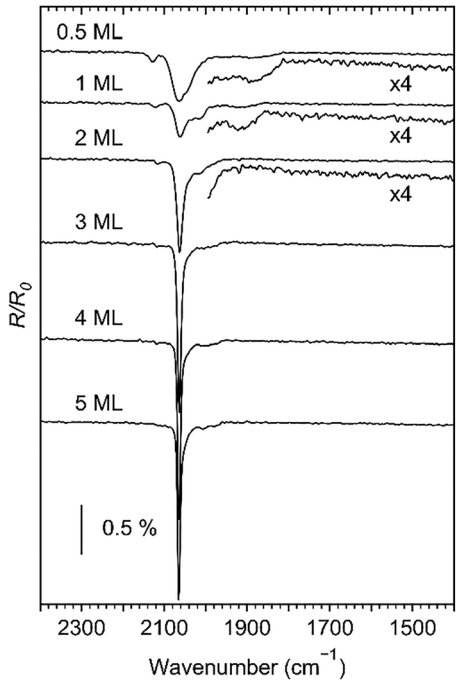

Fig. 5 RAIR spectra recorded after repeated dosing of $Fe(CO)_5$ onto a deposit prepared by EBID from $Fe(CO)_5$ and held at 115 K. The deposit was prepared as described in Section 3.2. *n* ML denotes the approximate number of $Fe(CO)_5$ monolayers adsorbed on the deposit after the given sequence of doses. A new background spectrum was recorded prior to each dosing.

Repeating the same dosing to obtain a coverage of 1 ML produced a RAIR spectrum in which the main band is sharpened. As a new background was recorded prior to each dosing and negative signals are absent, the spectrum is ascribed to the newly added molecules. A shoulder at 2016 cm^{-1} is assigned to the E'_{eq} vibration indicating a physisorbed species with its trigonal axis not exactly perpendicular to the surface and thus the beginning of multilayer growth (compare Section 3.1 and ref. 34). The $A'_{1,eq}$ band remains visible indicating that more molecules are added to the monolayer (Fig. 5, 1 ML). In contrast to the previous results for Fe surfaces,[23,24] however, the RAIR spectra recorded in the monolayer regime show broad bands around 1900 cm^{-1} (Fig. 5, 0.5 ML and 1 ML). This is considerably below the $\nu(C{\equiv}O)$ vibrational frequencies reported on Fe(110) and Fe(111) surfaces (see Section 3.1 and ref. 34) but falls within the typical range observed for bridging CO ligands.[41,42,45] This would indicate either the formation of complexes with more than one Fe (compare $Fe_2(CO)_9$, Section 3.1 and ref. 41) or a chemisorbed species in which CO ligands form bridges between the central atom of $Fe(CO)_5$ and surface Fe sites. Further dosing of $Fe(CO)_5$ produces the characteristic RAIR spectrum of multilayer $Fe(CO)_5$ adsorbates (Fig. 5, 2 ML and above), which is dominated by the strong and sharp $\nu(C{\equiv}O)$ band at 2065 cm^{-1}. This is consistent with previous data obtained for multilayer coverage.[19–25,34] The overall evolution of the RAIR spectra as function of coverage thus supports our monolayer calibration based on TDS data.[27,28]

To monitor the onset of possible thermal reactions, a 5 ML $Fe(CO)_5$ adsorbate (Fig. 6(a)) was annealed in steps of 50 K. RAIR spectra were recorded after each target temperature was reached and the heating was switched off (Fig. 6(b)). At 150 K, the intensity of the dominant $\nu(C{\equiv}O)$ band at 2065 cm^{-1} was reduced to roughly half of its initial value in line with the onset of multilayer desorption as observed in TDS.[27] At the same time, a new sharp band has developed at 2040 cm^{-1}. The intensity of the entire $\nu(C{\equiv}O)$ band system decreased strongly upon annealing to 200 K, where the RAIR spectrum of the $Fe(CO)_5$ monolayer was recovered (Fig. 6(c)). The intensity

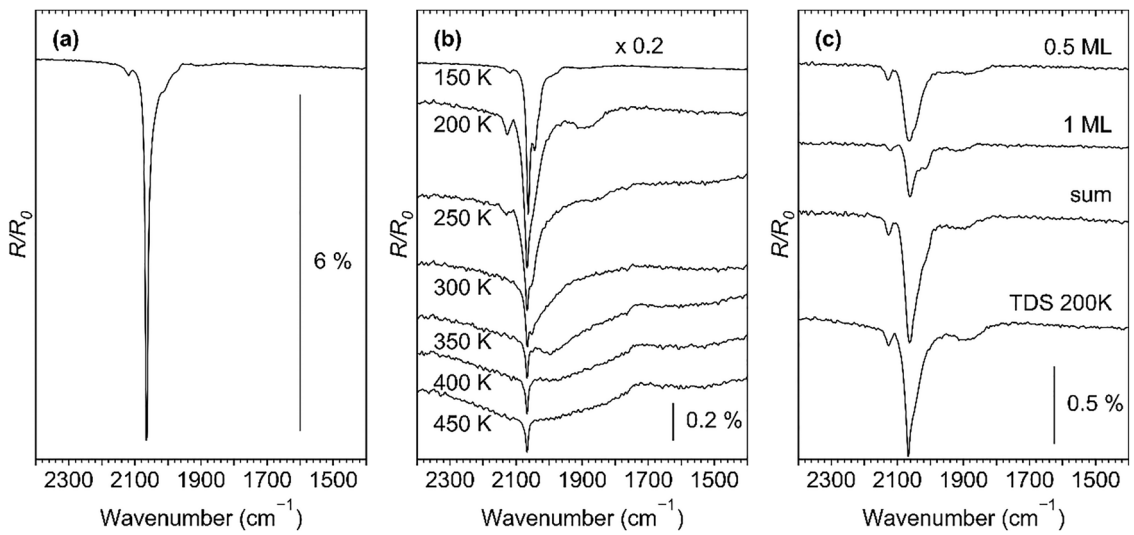

Fig. 6 (a) RAIR spectrum of a 5 ML $Fe(CO)_5$ adsorbate on a deposit prepared by EBID from $Fe(CO)_5$ and held at 115 K. (b) RAIR spectra of the same 5 ML $Fe(CO)_5$ adsorbate recorded after temperature increase in steps of 50 K. The same background spectrum recorded on the deposit was used to obtain all spectra in (a) and (b). (c) RAIR spectra from Fig. 5 recorded after the first two steps of $Fe(CO)_5$ dosing (0.5 ML and 1 ML) and sum therefore (sum) compared to the RAIR spectrum from (b) obtained after heating to 200 K.

decreased further at 250 K and 300 K indicating that $Fe(CO)_5$ was thermally decomposed. However, the resulting $\nu(C\equiv O)$ band is not broadened towards lower wavenumbers as was observed during the EBID process (Fig. 2). This implies a lower degree of Fe aggregation upon annealing of the $Fe(CO)_5$ multilayer without electron irradiation. This difference is rationalized by the fact that only monolayer quantities of $Fe(CO)_5$ were available for further thermal surface reactions after desorption of the multilayer while, during EBID, continued supply of precursor at room temperature provided enough material for formation of Fe aggregates.

It is tempting to assign the band at 2040 cm^{-1} observed at 150 K (Fig. 6(b)) to a reaction product. Formation of products such as $Fe_2(CO)_9$ or $Fe_3(CO)_{12}$ upon annealing was previously considered, but ruled out based on the argument that these complexes should be less volatile than $Fe(CO)_5$.[24] In fact, when a 3 ML adsorbate of $Fe(CO)_5$ on evaporated Fe was heated to 170 K, most of the intensity in RAIRS was lost except for a very small band at 2010 cm^{-1} that was tentatively ascribed to adsorbed CO.[24] To test these arguments, we have studied the adsorption at 115 K and desorption of $Fe_2(CO)_9$ by RAIRS. Only the sputtered Ta was used as substrate because the RAIRS data revealed that the sample of $Fe_2(CO)_9$ available to us contained significant quantities of an organic carbonyl-containing substance. Due to a much lower vapour pressure as compared to $Fe(CO)_5$, dosing was performed by leaving the valves open for an extended time while recording RAIR spectra. The data reveal the growth of a $\nu(C\equiv O)$ band system with dominant signals at 2000 cm^{-1} and 2030 cm^{-1} (SI, Fig. S4). This is significantly lower than the band positions reported for $Fe_2(CO)_9$ in an Ar matrix (2066 cm^{-1} and 2038 cm^{-1} (ref. 41)) and also compared to the 2040 cm^{-1} band observed upon annealing of $Fe(CO)_5$ (Fig. 6(b)). However, the band positions may not be exactly comparable due to the different environments ($Fe(CO)_5$ compared to Ar or the presence of an organic solvent) and coverages (compare also Section 3.1). The $\nu(C\equiv O)$ bands ascribed to $Fe_2(CO)_9$ decayed when the adsorbate was annealed above 170 K and disappeared above 190 K (SI, Fig. S5). This result alone does not allow us to rule out that the 2040 cm^{-1} band can be ascribed to a product such as $Fe_2(CO)_9$. We note, however, that previous TDS data monitoring the MS signal m/z 56 did not provide evidence for desorption of compounds containing Fe above 170 K.[27] Considering that $Fe_2(CO)_9$ is volatile enough to be dosed *via* the gas phase but has a significantly lower vapour pressure than $Fe(CO)_5$,[49] this casts strong doubts about the thermal formation of a polynuclear Fe complex prior to desorption of $Fe(CO)_5$.

An alternative explanation for the band at 2040 cm^{-1} is provided by our previous TDS results for $Fe(CO)_5$.[27] The data showed that while the second layer desorbed with a maximum desorption rate at 150 K, the desorption peak shifted to 165 K at coverages up to 5 ML.[27] This was ascribed to a crystallization process that requires a sufficient coverage. The constant position of the dominant $\nu(C\equiv O)$ band at 2065 cm^{-1} with increasing multilayer coverage as observed upon dosing of $Fe(CO)_5$ at 115 K (Fig. 5) indicates that this phase transition does not occur at liquid nitrogen temperature. In contrast, the new band at 2040 cm^{-1} that forms upon annealing of a 5 ML $Fe(CO)_5$ adsorbate likely relates to this new multilayer phase. An analogous interpretation was also derived from previous data for an $Fe(CO)_5$ adsorbate with coverage of about 3 ML on an evaporated Fe layer.[24] In this case, a red shift to 2053 cm^{-1} and broadening of the dominant $\nu(C\equiv O)$ band upon heating to 150 K was ascribed to the formation of a reconstructed multilayer based on the fact that the intensity of the band was still larger than for a monolayer.[24] The stronger red shift to 2040 cm^{-1} as observed herein (Fig. 6(b)) can relate to the higher initial coverage of 5 ML which, according to the previous TDS data,[24] leads to a more pronounced reconstruction or crystallization.

We note that a sharp peak at 2065 cm^{-1} remains visible with constant intensity up to 450 K. This is surprising considering that CO desorbs from a deposit prepared by EBID below 400 K and $\nu(C\equiv O)$ bands are consequently not observed anymore in RAIRS (Fig. 4). This latter result is consistent with previous RAIRS data for CO adsorbed on a fcc Fe(100) layer which showed a sharp signal near 2050 cm^{-1} at 102 K.[37] This signal shifted to lower wavenumbers at 175 K while spectra obtained above room temperature showed only bridging CO vibrations and the $\nu(C\equiv O)$ bands disappeared at 398 K.[37] Considering the coincidence with the dominant signal of $Fe(CO)_5$ (Fig. 6(a)) and noting that signals akin to those of the intact precursor were also seen in analogous experiments with $Fe(CO)_4MA$, we propose that the sharp peak at 2065 cm^{-1} relates to $Fe(CO)_5$ that had adsorbed on surfaces of the sample holder adjacent to the Ta sheet. These surfaces, which are not warming up together with the substrate, must have been accidentally hit by the IR beam. This interpretation is supported by the observation that such signals never occurred in experiments performed with the sample held at room temperature, a condition that would also disfavor accumulation of precursors on the sample holder.

As FEBID is typically performed at room temperature, it is particularly important to monitor the thermal surface chemistry of a precursor under the same conditions. Therefore, the same amount of $Fe(CO)_5$ as used to prepare deposits by EBID (Section 3.2) was dosed without electron irradiation onto a deposit held at room temperature. The progress of the surface reactions during dosing was monitored by RAIRS (Fig. 7). The spectra are similar to those obtained during the second EBID process shown in Fig. 2(c). A shoulder near 2060 cm^{-1} points to residual $Fe(CO)_5$. A broad band with maximum around 2000 cm^{-1} increased with ongoing dosing. However, bridging $\nu(C\equiv O)$ vibrations as observed for an $Fe(CO)_5$ monolayer at liquid nitrogen temperature (Fig. 5) were absent indicating that loss of CO is more pronounced at room temperature. As discussed in Section 3.2, the broad band around 2000 cm^{-1} (Fig. 7) gives evidence of thermal reactions leading to Fe aggregation upon contact of $Fe(CO)_5$ with the deposit surface. The continuous growth of this band reveals that this aggregation evolved as long as $Fe(CO)_5$ was dosed. The present RAIRS data thus visualize the autocatalytic deposit growth as

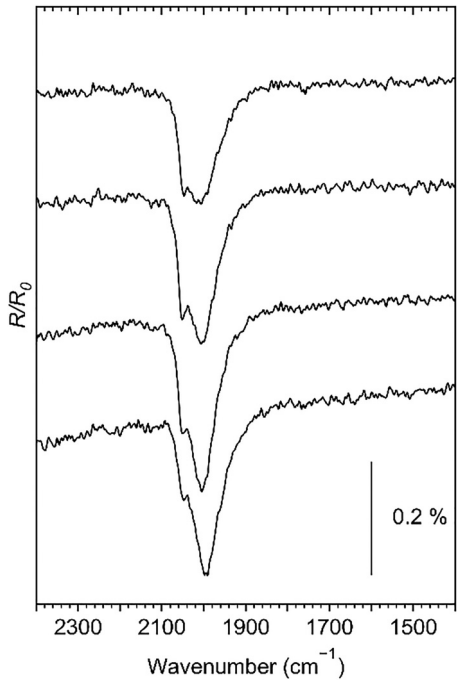

Fig. 7 RAIR spectra recorded during leaking of $Fe(CO)_5$ onto a deposit prepared by EBID from $Fe(CO)_5$ and held at room temperature. The total amount of $Fe(CO)_5$ vapour used in the experiment would have produced a 5 ML adsorbate at 115 K (see Section 2.3). Each spectrum represents a time interval of roughly 60 s with increasing deposition time from top to bottom. The last spectrum was recorded after dosing of $Fe(CO)_5$ was terminated. All RAIR spectra are referenced to a background recorded from the deposit prior to dosing of $Fe(CO)_5$.

demonstrated earlier by AES[27,28] and electron microscopy.[10,13] The result also supports that such autocatalytic growth unavoidably contributes to deposit formation during EBID from the $Fe(CO)_5$ precursor at room temperature.

3.4 Surface chemistry of $Fe(CO)_4A$ and $Fe(CO)_4MA$ on deposits prepared by EBID

The surface chemistry of $Fe(CO)_4A$ and $Fe(CO)_4MA$ on deposits prepared from $Fe(CO)_5$ by EBID was investigated as described in Section 3.3 for $Fe(CO)_5$. Small quantities of either $Fe(CO)_4A$ or $Fe(CO)_4MA$ were repeatedly dosed onto a deposit held at 115 K and a RAIR spectrum was recorded after each step (Fig. 8). The total amount of precursor vapour dosed in the experiment was sufficient to produce a 5 ML adsorbate according to previous TDS data[27,28] (see also Section 2.3). A new background spectrum was recorded prior to each dosing to visualize the different adsorption mode in the monolayer and the multilayers. An analogous experiment in which all RAIR spectra were referenced to the same background spectrum recorded prior to the first dosing is included in the SI (Fig. S6).

At multilayer coverage (Fig. 8, 2 ML and above), the RAIR spectra of $Fe(CO)_4A$ and $Fe(CO)_4MA$ are dominated by a strong and sharp band near 2050 cm^{-1} that is similar to the dominant $A''_{2,ax}$ signal of $Fe(CO)_5$ (see Sections 3.1 and 3.3). Due to the reduced molecular symmetry, bands near 2110 cm^{-1} and 2000 cm^{-1}, comparable to the $A'_{1,eq}$ and E'_{eq} vibrations of $Fe(CO)_5$, appear with medium intensity for both precursors. The strong shift of these main ν(C≡O) vibrations towards higher wavenumbers as compared to the solid phase (see SI, Fig. S7 and S8) gives again evidence of dipole coupling effects (compare Section 3.1). Additional bands of the organic ligands are present in the RAIR spectra with medium to weak intensity towards lower wavenumbers, the most prominent being the carbonyl ν(C═O) vibrations of the organic ligands A and MA at 1675 cm^{-1} ($Fe(CO)_4A$) and 1710 cm^{-1} ($Fe(CO)_4MA$), respectively.

At monolayer coverage (Fig. 8, 0.5 ML to 1 ML), the RAIR spectra of both $Fe(CO)_4A$ and $Fe(CO)_4MA$ differ distinctively from the multilayer spectrum. In both cases, the ν(C═O) vibration is absent (Fig. 8(a), 0.5 ML and 1 ML, Fig. 8(b), 0.5 ML) or has a very small intensity in the transition regime to the multilayer (Fig. 8(b), 1 ML). Instead, the spectra below 1800 cm^{-1} are dominated by a broad band around 1580 cm^{-1} in the case of $Fe(CO)_4A$ and 1620 cm^{-1} for $Fe(CO)_4MA$. This band is absent in the spectra of the intact precursors. It is tempting to ascribe this lack of ν(C═O) vibrations around 1700 cm^{-1} and the appearance of the band near 1600 cm^{-1} to a ν(C═O) vibration that is shifted by an interaction of the carbonyl group with the deposit surface. In fact, a strong red shift of the ν(C═O) band to 1435 cm^{-1} after desorption of the multilayers has been observed by HREELS for acrolein adsorbed on Rh(111) and ascribed to a η^2-type coordination of the carbonyl group to the metal surface.[50] We note that according to the surface selection rule,[35] ν(C═O) would be invisible in RAIRS if the carbonyl group was oriented exactly parallel to the metal surface as may be anticipated for a η^2-type coordination.[50] However, previous RAIRS data have shown that ν(C═O) of acrolein is visible and typically observed closer to 1700 cm^{-1} than to 1600 cm^{-1} for various metal surfaces (near 1700 cm^{-1} on Cu(111),[51] 1697 cm^{-1} and 1650 cm^{-1} on polycrystalline Cu,[52] 1690 cm^{-1} and 1663 cm^{-1} on Pd(111),[53] 1676 cm^{-1} on Ag(111),[54] 1700 cm^{-1} and 1662 cm^{-1} on Pt(111),[55] around 1700 cm^{-1} on Au(111) and polycrystalline Au[56]). In contrast, the ν(C═C) vibrations appear at wavenumbers closer to 1600 cm^{-1} but are generally weak.[51–56] The only exception is the Ru(001) surface where the ν(C═C) vibration of adsorbed acrolein was observed as a sharp band at 1631 cm^{-1} and more intense than ν(C═O) at 1689 cm^{-1} at lowest coverage.[57]

To support that the 1600 cm^{-1} band of monolayer $Fe(CO)_4A$ and $Fe(CO)_4MA$ adsorbates (Fig. 8) does not relate to a shifted ν(C═O) vibration, a reference experiment was performed by adsorbing increasing amounts of propanal on a deposit prepared from $Fe(CO)_5$ by EBID. Within the range of monolayer coverages, the RAIRS data show the ν(C═O) band at 1670 cm^{-1} (SI, Fig. S9). Additional bands at 1695 cm^{-1} and 1730 cm^{-1} grew with increasing multilayer coverage in close agreement with spectra obtained from solid propanal[58] as well as multilayers of propanal adsorbed on Pd(111)[53] and Ag(111).[54] Overall, the comparison with previous RAIR spectra of adsorbed acrolein[51–57] as well as the present data for propanal supports

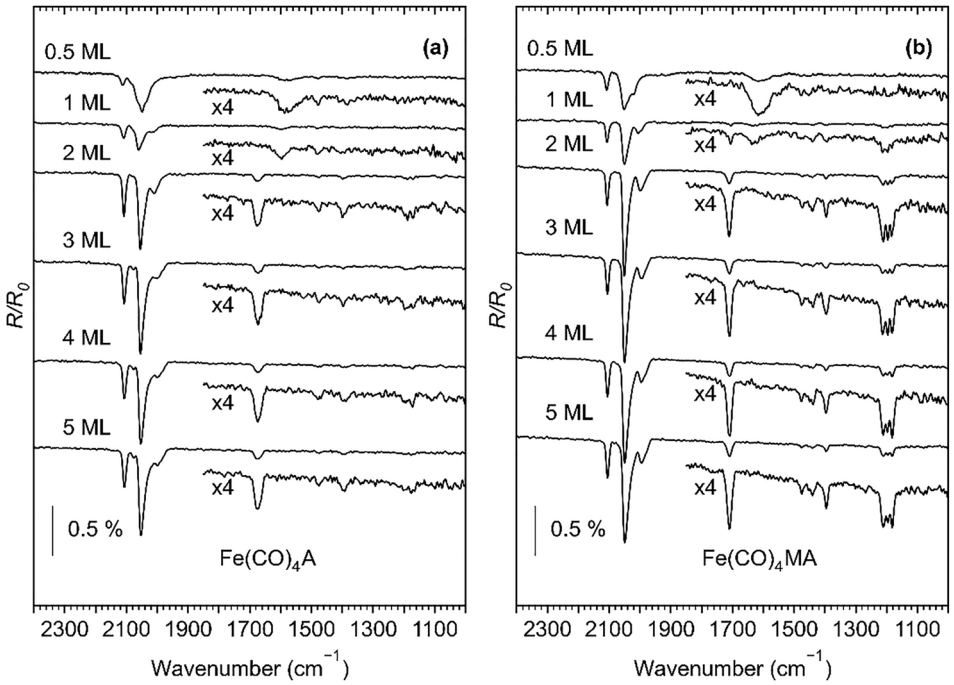

Fig. 8 RAIR spectra recorded after repeated dosing of (a) $Fe(CO)_4A$ and (b) $Fe(CO)_4MA$ onto deposits prepared by EBID from $Fe(CO)_5$ and held at 115 K. The deposits were prepared as described in Section 3.2. *n* ML denotes the approximate number of (a) $Fe(CO)_4A$ or (b) $Fe(CO)_4MA$ monolayers adsorbed on the deposit after the given sequence of doses. A new background spectrum was recorded prior to each dosing.

that the band around 1600 cm^{-1} (Fig. 8) cannot be ascribed to the ν(C═O) vibration of adsorbed $Fe(CO)_4A$ and $Fe(CO)_4MA$.

As previously proposed for $Fe(CO)_4MA$ on the basis of DFT calculations, loss of a CO ligand from the complex would lead to rearrangement of the MA ligand to a η^4-type coordination on the central Fe atom.[28] The same is conceivable for $Fe(CO)_4A$. This type of reaction has, in fact, been observed for $Fe(CO)_4MA$ in hexane solution.[59] However, the ν(C═O) vibration of the product $Fe(CO)_3MA$ was observed at 1511 cm^{-1} (ref. 59) and can thus also not explain the 1600 cm^{-1} band. As also shown by the previous calculations, the π-type coordination of the MA ligand to Fe is relatively weak in $Fe(CO)_4MA$.[28] Again, the situation should be similar for $Fe(CO)_4A$. Therefore, we may hypothesize that A and MA can be dissociated from the complex upon adsorption. If the ligand remained adsorbed on the surface, its unbound C═C unit should appear in the RAIR spectra with wavenumber closer to 1600 cm^{-1}.[51–57] However, the previous results[51–57] and the present data for adsorbed propanal (SI, Fig. S9) support that the ν(C═O) signal should then also be visible at wavenumbers closer to 1700 cm^{-1}. The complete lack of ν(C═O) signal at monolayer coverage (Fig. 8) thus argues against the presence of free A and MA ligands. Also, the ν(C≡O) band systems differ distinctly between $Fe(CO)_5$, $Fe(CO)_4A$, and $Fe(CO)_4MA$ even at monolayer coverage (Fig. 9). This indicates that the organic ligands or parts thereof still interact with the Fe of adsorbed $Fe(CO)_4A$ and $Fe(CO)_4MA$ precursors. We also note that bridging ν(C≡O) bands are absent or very weak in the RAIR spectra of $Fe(CO)_4A$ and $Fe(CO)_4MA$ at monolayer coverage (Fig. 9). This suggests that species derived from the A and MA ligands block coordination sites that would otherwise be involved in CO bridges.

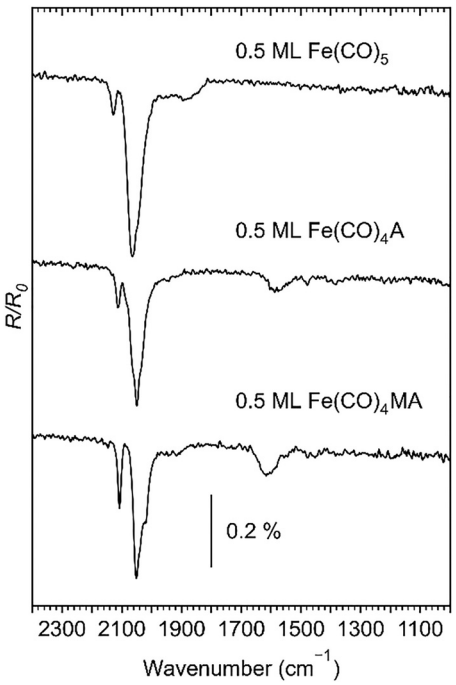

Fig. 9 Comparison of the RAIR spectra for submonolayer adsorbates of $Fe(CO)_5$, $Fe(CO)_4A$ and $Fe(CO)_4MA$ on deposits prepared by EBID from $Fe(CO)_5$ and held at 115 K. The deposits were prepared as described in Section 3.2. The spectra are assembled from Fig. 5 and 8.

The discussion so far indicates that intact A and MA ligands either bound to or dissociated from the precursor cannot explain the RAIR spectra obtained for monolayer adsorbates

of $Fe(CO)_4A$ and $Fe(CO)_4MA$ on the deposit prepared by EBID. For the sake of completeness, we briefly comment on the possibility of A and MA to polymerize on the deposit surface. In fact, free acrylate compounds are known to form polymers.[60,61] Also, an Fe-initiated radical polymerization has recently been reported.[60] Such reactions, however, typically convert the C═C double bonds to C–C single bonds while the carbonyl group remains intact with a ν(C═O) signal near the wavenumber for the monomer.[61] Therefore, a hypothetical surface-induced polymerization cannot explain the appearance of the 1600 cm^{-1} band.

The lack of ν(C═O) vibration in monolayer adsorbates of $Fe(CO)_4A$ and $Fe(CO)_4MA$ can be rationalized by dissociation of the ligand whereby the carbonyl group is lost. Focusing first on $Fe(CO)_4A$, we note that adsorbed acrolein has been observed to decarbonylate on different metal surfaces.[55,57,62,63] This reaction releases CO at temperatures at and above 280 K on Pt(111)[55] and above 230 K on Pd(110).[62,63] It has been proposed that the process is initiated by activation of the aldehyde C–H bond followed by extrusion of CO.[55] Also, catalytic activity of Ni nanoparticles towards decarbonylation of aldehydes has been reported.[64] Release of CO from the acrolein ligand would yield a C_2H_3 fragment with one possible structure being a vinyl radical. An Fe complex $(C_5H_5)Fe(CO)_2$–CH═CH_2 with vinyl bound to the Fe center *via* a σ bond has been reported with a strong vibrational band at 1560 cm^{-1}.[65] This is close to the 1580 cm^{-1} band for adsorbed monolayer $Fe(CO)_4A$, suggesting that vinyl σ-bonded to Fe within the dissociated complex or to the underlying surface can contribute to the observed spectrum. However, the broad nature of this band suggests that the fragmentation product is not a well-defined structure, but different binding situations are present. As one possibility, vinyl radicals may recombine to form a diene molecule. Such compounds have vibrational signals near 1600 cm^{-1} due to ν(C═C) vibrations but, as exemplified by data for 1,3-pentadiene (SI, Fig. S10), the sharp signals cannot explain the broad band observed for the adsorbed precursor molecules.

In the case of $Fe(CO)_4MA$, the aldehydic hydrogen of the A ligand is replaced by a methoxy group (OCH_3). In contrast to the situation for A, however, data on the adsorption and reactions of MA on surfaces are not available to the best of our knowledge. In analogy to the proposed C–H activation of A,[55] decarbonylation of MA would require loss of the methoxy group. Such a reaction might be driven by the affinity of Fe towards oxygen resulting in adsorbed methoxy species.[66] A study of the thermal decomposition of MA revealed expulsion of CO_2 as dominant reaction pathway.[67] Also, decarboxylation competes with decarbonylation for carboxylic acids adsorbed on metal surfaces[68,69] and in homogeneously catalyzed reactions[70] and is a preferred reaction pathway in catalytic conversion of aliphatic esters.[71,72] In both cases, vinyl would again be released from the MA ligand of $Fe(CO)_4MA$. The width of the 1620 cm^{-1} band and the shift compared to $Fe(CO)_4A$ (Fig. 9), however, point again to overlapping contributions from different products.

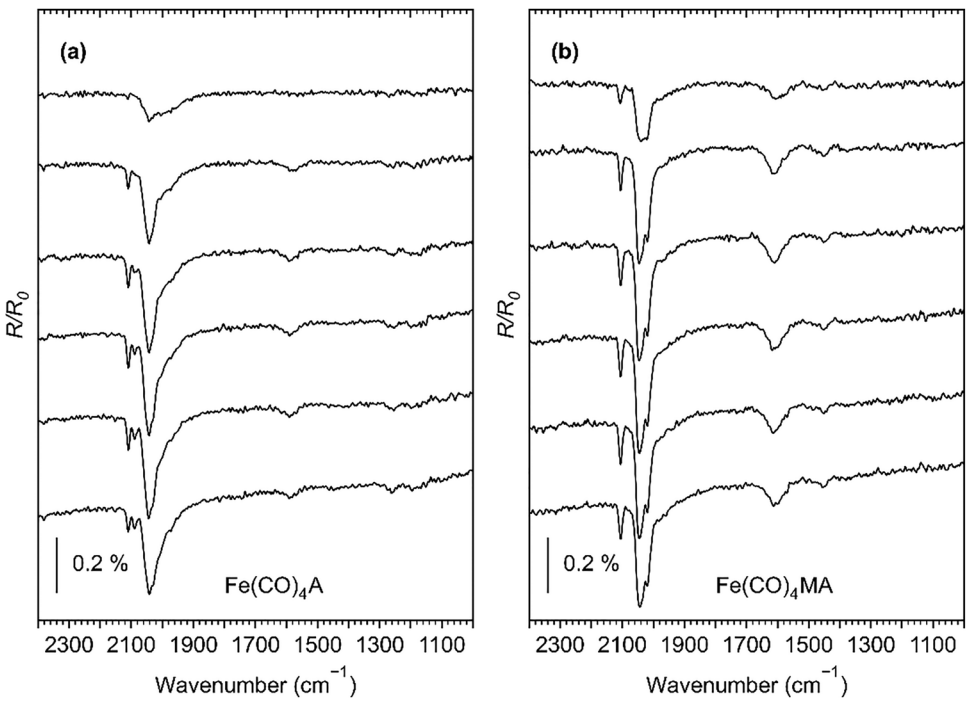

Fig. 10 RAIR spectra recorded during dosing of (a) $Fe(CO)_4A$ and (b) $Fe(CO)_4MA$ onto deposits prepared by EBID from $Fe(CO)_5$ and held at room temperature. The deposits were prepared as described in Section 3.2. The total amount of precursor vapour used in each frame would have produced a 5 ML adsorbate at 115 K (see Section 2.3). Each spectrum represents a time interval of roughly 60 s with increasing deposition time from top to bottom. The last spectrum was recorded after dosing of the precursor was terminated. All RAIR spectra are referenced to a background recorded from the deposit prior to dosing of the precursors.

In the case of $Fe(CO)_4MA$, this possibly includes carboxylate species that may be formed from the ester linkage and that have asymmetric stretching vibrations $\nu(CO_2)$ within this range of wavenumbers.[73]

Overall, we conclude from the monolayer RAIR spectra (Fig. 8 and 9) that the organic ligands of $Fe(CO)_4A$ and $Fe(CO)_4MA$ undergo surface-driven fragmentation when the precursors are adsorbed on the surface of a deposit prepared by EBID. The surprising result is that this reaction takes place at a temperature as low as 115 K. This is significantly lower than the temperatures at which decarbonylation of acrolein was observed.[55,62,63] Also, the present RAIR spectra (SI, Fig. S9) show that propanal does not decarbonylate at 115 K when adsorbed on an Fe deposit prepared by EBID. Therefore, we propose that coordination of A and MA to the $Fe(CO)_4$ moiety in $Fe(CO)_4A$ and $Fe(CO)_4MA$ activates the ligand so that the barrier towards decomposition is lowered.

The adsorption of $Fe(CO)_4A$ and $Fe(CO)_4MA$ on the deposit surface was also investigated at room temperature which is again particularly relevant to FEBID. As for $Fe(CO)_5$, the precursors were dosed on the deposit while repeatedly recording RAIR spectra (Fig. 10). The amount of precursor vapour dosed would have produced a 5 ML adsorbate at 115 K. At room temperature, the characteristic RAIR spectrum of the monolayer coverage (Fig. 9) appeared and saturated within three RAIRS scans in the case of $Fe(CO)_4A$ and within two RAIRS scans in the case of $Fe(CO)_4MA$ (Fig. 10). This implies that the products resulting from dissociation of the organic ligands upon adsorption on the deposit are stable enough to prevail at room temperature. Continued dosing did not lead to further changes in the spectra (Fig. 10), in contrast to the result for $Fe(CO)_5$ (Fig. 7). This suggests that the deposit surface was converted to a non-reactive state by adsorption of monolayer coverage of $Fe(CO)_4A$ and $Fe(CO)_4MA$. This conclusion is further substantiated in Section 3.5. As a subtle difference to the monolayer prepared at 115 K, the RAIR spectra of the $Fe(CO)_4A$ monolayer show an additional weak but sharp signal at 2090 cm^{-1} (Fig. 10(a)) pointing to reactions that are not accessible at 115 K. While it is tempting to assign this signal to species such as $Fe(CO)_4$, the summary of previous results (Section 3.1) supports that such assignments must be regarded with caution due to the lack of reliable reference data obtained from the same type of surface. It is interesting, though, to note that this band was not observed in the case of $Fe(CO)_4MA$ (Fig. 10(b)). This may relate to more extensive blocking of reactive surface sites by dissociation products of the larger MA ligand.

3.5 Deposition of Fe by thermal surface chemistry

The inhibition of thermal deposit growth by the organic ligands of $Fe(CO)_4A$ and $Fe(CO)_4MA$ as shown in Section 3.4 was also revealed by AES. To this end, the intensity of the Fe_{LMM} signal $I(Fe)$, normalized to the Ta_{NNN} signal of the freshly sputter-cleaned substrate $I_0(Ta)$, was evaluated after deposit formation by EBID and after subsequent thermal surface reactions initiated by dosing the precursors without electron irradiation. Each step of the experiments was performed by dosing an amount of precursor vapour that would have produced a 5 ML adsorbate on a surface held at 115 K (see Sections 2.3 and 3.4).

As discussed in Section 3.2, the deposits investigated herein are sufficiently thin to allow for a correlation between the quantity $I(Fe)/I_0(Ta)$ and the amount of deposited Fe, shown for ten individual experiments in Fig. 11. In all cases, the gray part of the bar represents the intensities obtained after deposit formation by EBID ($I_{EBID}(Fe)/I_0(Ta)$). The data are a subset of those shown in Fig. 3 (compare SI, Fig. S11) so that fluctuations of $I_{EBID}(Fe)/I_0(Ta)$ reflect the different amount of Fe deposited during the EBID process as consequence of the different duration of $Fe(CO)_5$ dosing (see SI, Table S1). The coloured parts of the bars represent the deposition of Fe by thermal surface reactions on the initial deposit. Green bars of experiments A and B reflect a single step of $Fe(CO)_5$ dosing. They reveal the increase of deposited Fe resulting from autocatalytic growth as also demonstrated by Fig. 7. In contrast, significantly less Fe was deposited in experiments C–J (red and blue bars). The red bars represent dosing of $Fe(CO)_4A$ (experiments C and D) or $Fe(CO)_4MA$ (experiments G and H) onto the initial deposit followed by dosing of $Fe(CO)_5$ without intermittent annealing. The blue bars represent experiments that included an additional electron irradiation step after dosing of $Fe(CO)_4A$ or

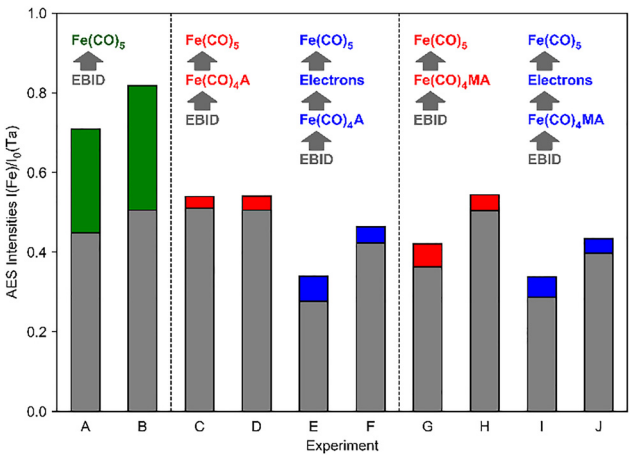

Fig. 11 Intensity of the Fe_{LMM} signal after one EBID step (gray bars) and after subsequent thermal surface reactions (coloured bars) normalized to the intensity of the Ta_{NNN} signal from the freshly sputtered surface prior to EBID for ten individual experiments (A)–(J). EBID was performed as described in Section 3.2. The height of the gray bars ($I_{EBID}(Fe)/I_0(Ta)$) vary as a result of different durations of $Fe(CO)_5$ dosing (see SI, Fig. S11 and Table S1). Thermal reactions were investigated by leaking the precursor onto the surface held at room temperature without performing electron irradiation. The green bars represent one thermal growth step performed by leaking $Fe(CO)_5$. The red bars represent two thermal growth steps performed by first leaking $Fe(CO)_4A$ or $Fe(CO)_4MA$ (see legend) followed by leaking of $Fe(CO)_5$ without intermittent annealing. The blue bars represent two thermal growth steps performed by first leaking $Fe(CO)_4A$ or $Fe(CO)_4MA$ (see legend) followed by electron irradiation (50 eV, 10 000 μC cm^{-2}) and then leaking of $Fe(CO)_5$ without intermittent annealing. The total amount of precursor vapour used for each deposit formation and in each thermal growth step of the experiments would have produced a 5 ML adsorbate at 115 K.

$Fe(CO)_4MA$ and before dosing of $Fe(CO)_5$, again without intermittent annealing. The rather small amount of deposited Fe in experiments C–J is in line with the lack of thermal growth at room temperature beyond the monolayer as deduced from the RAIRS data for $Fe(CO)_4A$ and $Fe(CO)_4MA$ (Section 3.4). However, the results also indicate that the adsorbed monolayer of $Fe(CO)_4A$ and $Fe(CO)_4MA$ efficiently blocks the surface to inhibit the thermal decomposition of $Fe(CO)_5$ which otherwise leads to continuous growth of Fe.[10,13,27,28]

We note that somewhat more Fe is thermally accumulated on particularly thin deposits (experiments E, G and I) as compared to other experiments from group C–J (Fig. 11). This result can be rationalized by considering that the average thickness of the Fe deposit produced by EBID is below five atomic layers. This estimate results from the fact that the amount of precursor vapour dosed onto the surface during EBID corresponds to a thickness of 5 ML when adsorbed at 115 K. At such low thickness, formation of small aggregates is more likely than a continuous layer with homogeneous thickness.[28] Particularly small amounts of deposited Fe as obtained in the EBID step of experiments E, G, and I would thus signify that those aggregates are also smaller than in the other experiments. In consequence, they may be more reactive leading to somewhat more Fe being deposited in the thermal growth step.

The progress of deposition during the experiments summarized by Fig. 11 was also monitored by RAIRS. Fig. 12 and 13 show representative data for $Fe(CO)_4A$ and $Fe(CO)_4MA$, respectively. The top spectrum in each frame was recorded after dosing of the precursors onto a deposit prepared by EBID from $Fe(CO)_5$ and held at room temperature. The spectra agree reasonably well with the data of Fig. 10 except for a somewhat higher noise level that masks the weaker 1600 cm^{-1} band in the case of $Fe(CO)_4A$ (Fig. 12(a)). RAIRS data obtained upon subsequent dosing of $Fe(CO)_5$ without intermittent annealing are shown at the bottom of Fig. 12(a) for $Fe(CO)_4A$ and of Fig. 13(a) for $Fe(CO)_4MA$. In both cases, a new background spectrum was recorded prior to dosing of $Fe(CO)_5$. The absence of $\nu(C\equiv O)$ bands indicates that $Fe(CO)_5$ did not adsorb on the deposit precovered by the chemisorbed monolayers of $Fe(CO)_4A$ or $Fe(CO)_4MA$. This explains the lack of autocatalytic deposit growth in experiments C, D, G, and H (Fig. 11).

RAIRS data representing selected experiments from the group E, F, I, and J in Fig. 11 are shown in Fig. 12(b) and 13(b). The same background recorded prior to dosing of $Fe(CO)_4A$ and $Fe(CO)_4MA$, respectively, was used throughout these experiments. The RAIR spectra below the spectrum of the chemisorbed monolayers were recorded during and after electron irradiation which lead to rapid decay of all signals. Despite this, subsequent dosing of $Fe(CO)_5$ produced only small $\nu(C\equiv O)$ bands as compared to Fig. 7 indicating that electron irradiation has not efficiently removed the material originating from $Fe(CO)_4A$ and $Fe(CO)_4MA$. From the absence of signals after electron irradiation, we propose that the species resulting from reactive adsorption of $Fe(CO)_4A$ and $Fe(CO)_4MA$ have been converted to a layer that was invisible in RAIRS. This layer

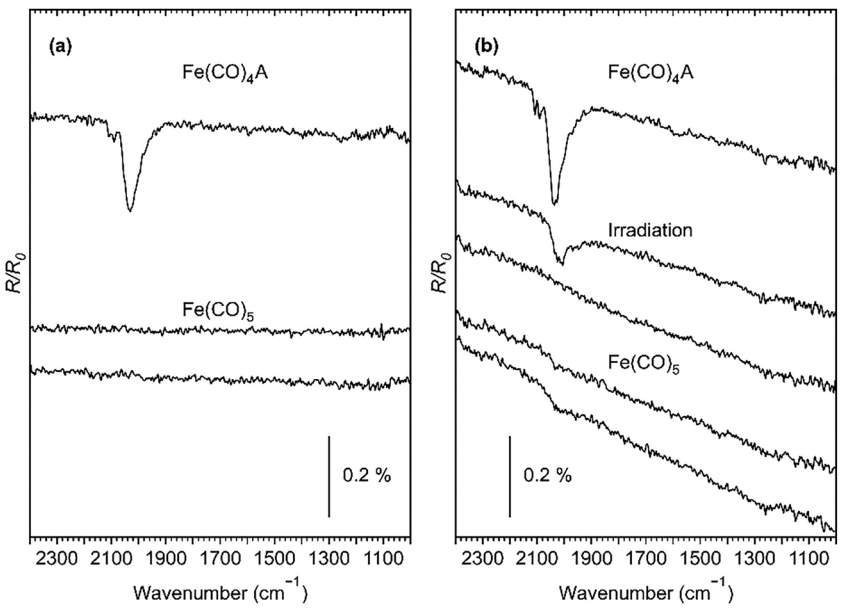

Fig. 12 (a) From top to bottom: RAIRS after dosing of $Fe(CO)_4A$ onto a deposit prepared by EBID from $Fe(CO)_5$ and held at room temperature with background recorded from the deposit prior to dosing. First RAIRS recorded during subsequent dosing of $Fe(CO)_5$ and RAIRS after completion of $Fe(CO)_5$ dosing. The background used for the latter two spectra was recorded after dosing of $Fe(CO)_4A$. (b) From top to bottom: RAIRS recorded after dosing of $Fe(CO)_4A$ onto a deposit prepared by EBID from $Fe(CO)_5$ and held at room temperature. First RAIRS recorded during subsequent electron irradiation (50 eV, 10 000 μC cm^{-2}) and RAIRS after irradiation. First RAIRS recorded during subsequent dosing of $Fe(CO)_5$ and RAIRS after completion of $Fe(CO)_5$ dosing. All spectra in (b) were referenced to a background recorded from the deposit prior to dosing of $Fe(CO)_4A$. The deposits were prepared as described in Section 3.2. The total amount of precursor vapour in each of the dosing steps would have produced a 5 ML adsorbate at 115 K (see Section 2.3). Each spectrum represents a time interval of roughly 60 s.

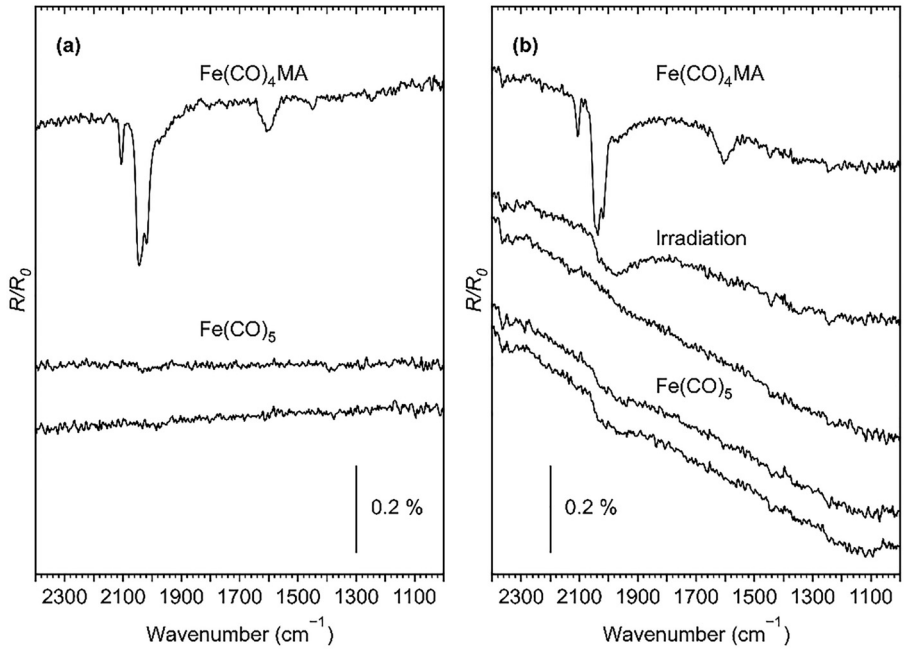

Fig. 13 (a) From top to bottom: RAIRS after dosing of $Fe(CO)_4MA$ onto a deposit prepared by EBID from $Fe(CO)_5$ and held at room temperature with background recorded from the deposit prior to dosing. First RAIRS recorded during subsequent dosing of $Fe(CO)_5$ and RAIRS after completion of $Fe(CO)_5$ dosing. The background used for the latter two spectra was recorded after dosing of $Fe(CO)_4MA$. (b) From top to bottom: RAIRS recorded after dosing of $Fe(CO)_4MA$ onto a deposit prepared by EBID from $Fe(CO)_5$ and held at room temperature. First RAIRS recorded during subsequent electron irradiation (50 eV, 10 000 μC cm^{-2}) and RAIRS after irradiation. First RAIRS recorded during subsequent dosing of $Fe(CO)_5$ and RAIRS after completion of $Fe(CO)_5$ dosing. All spectra in (b) were referenced to a background recorded from the deposit prior to dosing of $Fe(CO)_4A$. The deposits were prepared as described in Section 3.2. The total amount of precursor vapour in each of the dosing steps would have produced a 5 ML adsorbate at 115 K (see Section 2.3). Each spectrum represents a time interval of roughly 60 s.

possibly consisted of carbon species that cannot be further specified here. In line with the AES data of experiments E, F, I, and J in Fig. 11, this material efficiently blocks surface sites of the deposit that would be needed to induce autocatalytic reactions of $Fe(CO)_5$.

4 Conclusions

The thermal reactions of $Fe(CO)_4A$ and $Fe(CO)_4MA$ that occur upon adsorption on an Fe deposit produced by EBID differ distinctively from those of $Fe(CO)_5$. This is revealed by the results of RAIRS experiments. RAIRS is a powerful tool of surface chemistry but has so far not been used extensively to investigate the surface chemistry of FEBID precursors. $Fe(CO)_5$ sustains continuous autocatalytic growth upon dosing onto the surface. This is apparent from a red shift and broadening of the characteristic $\nu(C\equiv O)$ bands with increasing gas dose. In contrast, $Fe(CO)_4A$ and $Fe(CO)_4MA$ undergo dissociative adsorption at monolayer coverage even at 115 K. This reaction leads to fragmentation of the ligands A and MA with products that persist on the surface at room temperature and thus prevent further adsorption of precursor molecules. This surface poisoning efficiently suppresses autocatalytic thermal growth of Fe deposits during subsequent dosing of $Fe(CO)_5$. It also explains the lack of autocatalytic growth as observed previously for $Fe(CO)_4MA$[28] and herein also for $Fe(CO)_4A$. As shown previously,[28] deposits prepared by EBID from $Fe(CO)_4MA$ contain significantly less carbon than anticipated from the stoichiometry of the precursor. The modified precursors $Fe(CO)_4A$ and $Fe(CO)_4MA$ thus offer the perspective to improve shape control in FEBID processes as compared to $Fe(CO)_5$ by avoiding thermal autocatalytic growth while at the same time, as shown previously for $Fe(CO)_4MA$,[28] yielding a similar deposit composition as is the case for $Fe(CO)_5$.

Author contributions

Lars Barnewitz: data curation; formal analysis; investigation; validation; visualization; writing – review & editing. Hannah Boeckers: investigation; visualization; writing – review & editing. Atul Chaudhary: investigation; validation; writing – review & editing. Lisa McElwee-White: conceptualization; funding acquisition; supervision; writing – review & editing. Petra Swiderek: conceptualization; funding acquisition; supervision; writing – original draft preparation; writing – review & editing.

Conflicts of interest

There are no conflicts to declare.

Data availability

Supplementary information (SI) is available. SI features coverage-dependent TDS data for $Fe(CO)_4A$ (Fig. S1), AES data of the Ta sheet and a deposit prepared by EBID (Fig. S2), coverage-dependent RAIRS of $Fe(CO)_5$ (Fig. S3), RAIRS of adsorbed $Fe_2(CO)_9$ (Fig. S4 and S5), coverage-dependent RAIRS of $Fe(CO)_4A$ and $Fe(CO)_4MA$ (Fig. S6), ATR-IR spectra of $Fe(CO)_4A$ (Fig. S7) and $Fe(CO)_4MA$ (Fig. S8), coverage-dependent RAIRS of propanal (Fig. S9), coverage-dependent RAIRS of 1,3-pentadiene (Fig. S10), plot and table of normalized AES Fe_{LMM} intensity as function of the duration of $Fe(CO)_5$ dosing during EBID (Fig. S11 and Table S1). See DOI: https://doi.org/10.1039/d6cp00492j.

Raw data for this article are available at [zenodo] at [https://doi.org/10.5281/zenodo.19351794].

Acknowledgements

P. S. and L. B. thank the DFG for funding under grant 529947802. L. M.-W. and A. C. thank the National Science Foundation for support under grant CHE-2404057.

References

1 I. Utke, P. Hoffmann and J. Melngailis, *J. Vac. Sci. Technol., B*, 2008, **26**, 1197.
2 M. Huth, F. Porrati and O. V. Dobrovolskiy, *Microelectron. Eng.*, 2018, **185–186**, 9.
3 I. Utke, P. Swiderek, K. Höflich, K. Madajska, J. Jurczyk, P. Martinović and I. B. Szymańska, *Coord. Chem. Rev.*, 2022, **458**, 213851.
4 V. Reisecker, R. Winkler and H. Plank, *Adv. Funct. Mater.*, 2024, **34**, 2407567.
5 R. M. Thorman, T. P. Ragesh Kumar, D. H. Fairbrother and O. Ingólfsson, *Beilstein J. Nanotechnol.*, 2015, **6**, 1904.
6 W. G. Carden, H. Lu, J. A. Spencer, D. H. Fairbrother and L. McElwee-White, *MRS Commun.*, 2018, **8**, 343.
7 S. Barth, M. Huth and F. Jungwirth, *J. Mater. Chem. C*, 2020, **8**, 15884.
8 J.-C. Yu, M. K. Abdel-Rahman, D. H. Fairbrother and L. McElwee-White, *ACS Appl. Mater. Interfaces*, 2021, **13**, 48333.
9 F. Tu, M. Drost, F. Vollnhals, A. Späth, E. Carrasco, R. H. Fink and H. Marbach, *Nanotechnology*, 2016, **27**, 355302.
10 T. Lukasczyk, M. Schirmer, H.-P. Steinrück and H. Marbach, *Langmuir*, 2009, **25**, 11930.
11 H. Marbach, *Appl. Phys. A: Mater. Sci. Process.*, 2014, **117**, 987.
12 M. Drost, F. Tu, F. Vollnhals, I. Szenti, J. Kiss and H. Marbach, *Small Methods*, 2017, **1**, 1700095.
13 G. Hochleitner, H. D. Wanzenboeck and E. Bertagnolli, *J. Vac. Sci. Technol., B*, 2008, **26**, 939.
14 A. Tsarapkin, K. Maćkosz, C. S. Jureddy, I. Utke and K. Höflich, *Adv. Mater.*, 2024, **36**, 2313571.
15 N. P. Jochmann, A. Salvador-Porroche and S. Barth, *Adv. Funct. Mater.*, 2025, **35**, e07465.
16 F. Porrati, S. Barth, G. C. Gazzadi, S. Frabboni, O. M. Volkov, D. Makarov and M. Huth, *ACS Nano*, 2023, **17**, 4704.
17 B. B. Lewis, B. A. Mound, B. Srijanto, J. D. Fowlkes, G. M. Pharr and P. D. Rack, *Nanoscale*, 2017, **9**, 16349.
18 K. Höflich, K. Maćkosz, C. S. Jureddy, A. Tsarapkin and I. Utke, *Beilstein J. Nanotechnol.*, 2024, **15**, 1117.
19 F. Zaera, *Surf. Sci.*, 1991, **255**, 280.
20 S. Sato and T. Suzuki, *J. Phys. Chem.*, 1996, **100**, 14769.
21 S. Sato and S. Tanaka, *Appl. Surf. Sci.*, 1998, **135**, 83.
22 S. Sato, S. Minoura, T. Urisu and Y. Takasu, *Appl. Surf. Sci.*, 1995, **90**, 29.
23 T. Tanabe, K. Kubo, T. Ishibashi, T. Wadayama and A. Hatta, *Appl. Surf. Sci.*, 2003, **207**, 115.
24 T. Tanabe, T. Morisato, Y. Suzuki, Y. Matsumoto, T. Wadayama and A. Hatta, *Vib. Spectrosc.*, 1998, **18**, 141.
25 S. Sato, Y. Ukisu, H. Ogawa and Y. Takasu, *J. Chem. Soc., Faraday Trans.*, 1993, **89**, 4387.
26 F. Zaera, *Coord. Chem. Rev.*, 2013, **257**, 3177.
27 P. Martinović, L. Barnewitz, M. Rohdenburg and P. Swiderek, *J. Vac. Sci. Technol., A*, 2023, **41**, 033207.
28 H. Boeckers, A. Chaudhary, P. Martinović, A. V. Walker, L. McElwee-White and P. Swiderek, *Beilstein J. Nanotechnol.*, 2024, **15**, 500.
29 H. Boeckers, M. Rohdenburg and P. Swiderek, *Surf. Sci.*, 2025, **751**, 122628.
30 J. D. Wnuk, S. G. Rosenberg, J. M. Gorham, W. F. van Dorp, C. W. Hagen and D. H. Fairbrother, *Surf. Sci.*, 2011, **605**, 257.
31 P. Iyngaran, D. C. Madden, D. A. King and S. J. Jenkins, *J. Phys. Chem. C*, 2017, **121**, 24594.
32 E. Weiss, K. Stark, J. E. Lancaster and H. D. Murdoch, *Helv. Chim. Acta*, 1963, **46**, 288.
33 M. Bigorgne, *J. Organomet. Chem.*, 1970, **24**, 211.
34 C. Hauchard, C. Pépin and P. Rowntree, *Langmuir*, 2005, **21**, 9154.
35 A. M. Bradshaw and E. Schweizer, in *Spectroscopy of Surfaces*, ed. R. J. H. Clark and R. E. Hester, Wiley, New York, 1988, pp. 413–483.
36 S. Ishi, Y. Ohno and B. Viswanathan, *Surf. Sci.*, 1985, **161**, 349.
37 T. Tanabe, Y. Suzuki, T. Wadayama and A. Hatta, *Surf. Sci.*, 1999, **427–428**, 414.
38 J. M. Parnis, M. G. K. Thompson and L. M. Ashenhurst, *J. Phys. Chem. A*, 2003, **107**, 7390.
39 J. Lengyel, P. Papp, Š. Matejčík, J. Kočišek, M. Fárník and J. Fedor, *Beilstein J. Nanotechnol.*, 2017, **8**, 2200.
40 M. Allan, M. Lacko, P. Papp, Š. Matejčík, M. Zlatar, I. I. Fabrikant, J. Kočišek and J. Fedor, *Phys. Chem. Chem. Phys.*, 2018, **20**, 11692.
41 M. Poliakoff and J. J. Turner, *J. Chem. Soc. A*, 1971, 2403.
42 D. M. Adams and I. D. Taylor, *J. Chem. Soc., Faraday Trans. 2*, 1982, **78**, 1551.
43 M. R. Trushelm and R. L. Jackson, *J. Phys. Chem.*, 1983, **87**, 1910.

44 M. Poliakoff and J. J. Turner, *J. Chem. Soc. D: Chem. Commun.*, 1970, 1008.
45 A. Fielicke, *Chem. Soc. Rev.*, 2023, **52**, 3778.
46 J. M. Rall, M. Schorpp, M. Keilwerth, M. Mayländer, C. Friedmann, M. Daub, S. Richert, K. Meyer and I. Krossing, *Angew. Chem., Int. Ed.*, 2022, **61**, e202204080.
47 M. Zhou, G. V. Chertihin and L. Andrews, *J. Chem. Phys.*, 1998, **109**, 10893.
48 M. Zhou and L. Andrews, *J. Chem. Phys.*, 1999, **110**, 10370.
49 J. Watt, G. C. Bleier, M. J. Austin, S. A. Ivanov and D. L. Huber, *Nanoscale*, 2017, **9**, 6632.
50 N. F. Brown and A. Barteau, *J. Am. Chem. Soc.*, 1992, **114**, 4258.
51 A. Islam, D. L. Molina and M. Trenary, *Phys. Chem. Chem. Phys.*, 2022, **24**, 2483.
52 M. T. Nayakasinghe, R. Ponce Perez, B. Chen, N. Takeuchi and F. Zaera, *J. Catal.*, 2022, **414**, 257.
53 K.-H. Dostert, C. P. O'Brien, F. Mirabella, F. Ivars-Barceló and S. Schauermann, *Phys. Chem. Chem. Phys.*, 2016, **18**, 13960.
54 M. Muir, D. L. Molina, A. Islam, M. K. Abdel-Rahman and M. Trenary, *Phys. Chem. Chem. Phys.*, 2020, **22**, 25011.
55 J. C. de Jesús and F. Zaera, *Surf. Sci.*, 1999, **430**, 99.
56 M. Akita, N. Osaka and K. Itoh, *Surf. Sci.*, 1998, **405**, 172.
57 D. A. Esan, Y. Ren, X. Feng and M. Trenary, *J. Phys. Chem. C*, 2017, **121**, 4384.
58 Y. Y. Yarnall, P. A. Gerakines and R. L. Hudson, *Mon. Not. R. Astron. Soc.*, 2020, **494**, 4606.
59 S. Muhammad, S. Moncho, B. Li, S. J. Kyran, E. N. Brothers, D. J. Darensbourg and A. A. Bengali, *Inorg. Chem.*, 2013, **52**, 12655.
60 B. Palucci, A. Vignali, F. Bertini and S. Losio, *Polym. Chem.*, 2025, **16**, 4120.
61 S. H. Kandil and M. A. El-Gamal, *J. Polym. Sci., Part A:Polym. Chem.*, 1986, **24**, 2765.
62 R. Shekhar and M. A. Barteau, *Surf. Sci.*, 1994, **319**, 298.
63 K.-H. Dostert, C. P. O'Brien, F. Ivars-Barceló, S. Schauermann and H.-J. Freund, *J. Am. Chem. Soc.*, 2015, **137**, 13496.
64 T. Matsuyama, T. Yatabe, T. Yabe and K. Yamaguchi, *ACS Catal.*, 2021, **11**, 13745.
65 M. L. H. Green, M. Ishaq and T. Mole, *Z. Naturforsch. B*, 1965, **20**, 598.
66 G.-C. Wang, Y.-H. Zhou and J. Nakamura, *J. Chem. Phys.*, 2005, **122**, 044707.
67 R. L. Forman, H. M. Mackinnon and P. D. Ritchie, *J. Chem. Soc.*, 1968, 2013.
68 K. C. Chukwu and L. Árnadóttir, *J. Phys. Chem. C*, 2020, **124**, 13082.
69 J. Lu, S. Behtash and A. Heyden, *J. Phys. Chem. C*, 2012, **116**, 14328.
70 Z. Huang, M. E. Akana, K. M. Sanders and D. J. Weix, *Science*, 2024, **385**, 1331.
71 J. Han, H. Sun, Y. Ding, H. Lou and X. Zheng, *Green Chem.*, 2010, **12**, 463.
72 X. Cao, F. Long, F. Wang, J. Zhao, J. Xu and J. Jiang, *Renewable Energy*, 2021, **180**, 1.
73 G. B. Deacon and R. J. Phillips, *Coord. Chem. Rev.*, 1980, **33**, 227.